

4

Precursory Vehicle Modelling

4.1 Background

In Chapter 2 we studied several examples that introduce the underlying mechanics ideas required for road vehicle modelling. Predominant is the mechanics of the rolling contact that was studied in the context of the rolling ball (Section 2.9) and the rolling disc (Section 2.10). Our study of these examples made extensive use of (pure) non-slip rolling idealizations, in which any material point on the surface of the rolling ball, or the periphery of the rolling disc, which is in (instantaneous) contact with a stationary base surface is assumed stationary. These conditions are enforced by a pair of nonholonomic constraints—typically in two non-parallel ground-plane directions. The contact modelling is completed by a holonomic constraint in the vertical direction; see for example (2.234) and (2.235), and (2.264).

By the 1950s, the understanding of tyre and rolling-contact behaviour had improved substantially and it had become commonplace, although not universal, to regard the rolling contact as a force producer rather than a motion constraint [83]. In this abstraction the rolling-contact material at the ground plane ‘slips’ relative to the rolling surface and so has a non-zero absolute velocity. Under these conditions the linkage between the rolling body’s rotational and translational velocities is lost. To model this slip-dependent behaviour it is necessary to introduce a slip-dependent force-generation mechanism, which might be an elementary description of the type given in (2.255) and (2.256), or a more sophisticated description of the type given in Chapter 3. These slip mechanisms can have a substantial impact on the dynamics of most vehicles. They can also produce new slip-related phenomena that can be highly undesirable. Obvious among these are skidding tyres; less obvious are various unstable oscillatory phenomena that we will study here, with more extensive treatments appearing in later chapters.

The focus of this chapter will be on precursory car and bicycle models, and an oscillatory phenomenon commonly referred to as ‘shimmy’. In a subsequent chapters the single-track models introduced here will be developed into fully fledged bicycle and motorcycle models, while shimmy-related phenomena will reappear in the context of both bicycle and motorcycle dynamics.

4.2 Simple car model

Some of the fundamental properties of road cars can be developed with the help of simple single-track models of the type shown in Figure 4.1. In entry-level models of this type, many influences such as the suspension dynamics, chassis and tyre compliances, and lateral load transfer effects are ignored.

In the figure the car's wheelbase is given by w ; a and b locate the vehicle's mass centre relative to the wheel ground contacts; u and v ($v < 0$ in figure) are, respectively, the longitudinal and lateral components of the car's mass centre velocity \mathbf{V} ; ν locates the vehicle's neutral steer point which is defined below; δ is the car's steering angle; α_f and α_r are, respectively, the front and rear tyre side-slip angles (which are defined in (3.7) and lie between the tyre centre velocity and the tyre longitudinal axis); β ($\beta < 0$ in the figure) is the vehicle side-slip angle (that lies between the vehicle mass centre velocity \mathbf{V} and the vehicle's longitudinal axis); F_{fy} and F_{ry} are, respectively, the tyres' front and rear lateral forces; F_{fx} and F_{rx} are the front- and rear-tyre longitudinal drive or brake forces (not shown); ω is the car's yaw velocity; a_y is the car mass centre's lateral acceleration; and \mathcal{R} is the mass centre's radius of curvature, herein defined as the distance between the mass centre G and the instantaneous centre of rotation C .

The exact nature of the lateral acceleration a_y and the radius of curvature \mathcal{R} require further analysis. The velocity of the car's mass centre (in body-fixed coordinates) is $\mathbf{V} = u\mathbf{i} + v\mathbf{j}$, and so the lateral acceleration is given by $d\mathbf{V}/dt = \dot{\mathbf{V}} + \omega\mathbf{k} \times \mathbf{V}$, where $\dot{\mathbf{V}}$ refers to the component-wise derivative. In particular $d\mathbf{V}/dt = \hat{a}_x\mathbf{i} + \hat{a}_y\mathbf{j}$, with $\hat{a}_x = \dot{u} - \omega v$ and $\hat{a}_y = \dot{v} + \omega u$; \hat{a}_y is the lateral acceleration normal to the car's plane of symmetry. In contrast, the lateral acceleration a_y depicted in Figure 4.1 is normal to the velocity \mathbf{V} and is given by $a_y = (\omega + \dot{\beta})V$. Under steady-state conditions the two

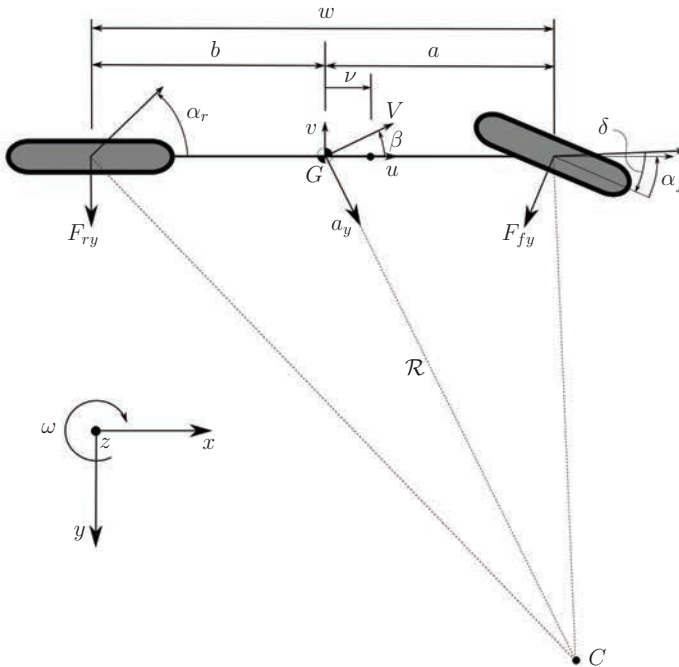


Figure 4.1: Kinematics of a single-track car model showing its basic geometric parameters. Also shown are the reference axes.

expressions become $\hat{a}_y^{ss} = \omega u$ and $a_y^{ss} = \omega V$. Under normal driving conditions, with a small side-slip angle, $\hat{a}_y \approx a_y$. The *velocity centre* or *instantaneous centre of rotation* C is obtained using (2.146) by setting $\mathbf{V} + \omega \mathbf{k} \times \mathbf{r}_C = \mathbf{0}$, which gives the location of point C as $\mathbf{r}_C = -\frac{v}{\omega} \mathbf{i} + \frac{u}{\omega} \mathbf{j}$. The distance between C and the symmetry plane of the car is $\hat{\mathcal{R}} = \frac{u}{\omega}$, which is in contrast to the distance $\mathcal{R} = V/(\omega + \beta)$ between C and G depicted in Figure 4.1. Again, under normal driving conditions, the two are very close and $\hat{\mathcal{R}} \approx \mathcal{R}$ for small angles. In general C does not coincide with the *acceleration centre*, which is the point with zero acceleration; the two centres do coincide under steady turning.

Balancing forces in the longitudinal and lateral directions, and balancing yaw moments around the car's mass centre, give the following well-known equations of motion (EOMs):¹

$$m\dot{u} = m\omega v - F_{fy} \sin \delta + F_{fx} \cos \delta + F_{rx}, \quad (4.1)$$

$$m\dot{v} = -m\omega u + F_{fy} \cos \delta + F_{fx} \sin \delta + F_{ry}, \quad (4.2)$$

$$J\dot{\omega} = a(F_{fy} \cos \delta + F_{fx} \sin \delta) - bF_{ry}, \quad (4.3)$$

in which m and J are, respectively, the car's mass and yaw moment of inertia; the model's state variables are u , v , and ω .

The three side-slip angles are computed using the kinematic relationships:

$$\beta = \arctan\left(\frac{v}{u}\right), \quad (4.4)$$

$$\alpha_f = \delta - \arctan\left(\frac{\omega a + v}{u}\right), \quad (4.5)$$

$$\alpha_r = \arctan\left(\frac{\omega b - v}{u}\right). \quad (4.6)$$

The following small-angle approximations are often used:

$$\beta = \frac{v}{u}, \quad (4.7)$$

$$\alpha_f = \delta - \frac{\omega a + v}{u}, \quad (4.8)$$

$$\alpha_r = \frac{\omega b - v}{u}. \quad (4.9)$$

Another classic assumption in the single-track car model is that the longitudinal velocity u is given and fixed. In this case (4.1) can be neglected and the system is described by v and ω only.² If it is further assumed that the vehicle is rear-wheel drive (RWD), and that the rolling resistance at the front wheel is negligible ($F_{fx} = 0$), the equations of motion simplify to the following classic form

¹ These equations are easily derived using (2.76), (2.77), and (2.78), with $\mathcal{L} = \frac{m}{2}(u^2 + v^2) + \frac{J}{2}\omega^2$.

² The term $m\omega v$ in (4.1) can also be neglected for small ω and v .

$$m\dot{v} = -m\omega u + F_{fy} + F_{ry} \quad (4.10)$$

$$J\dot{\omega} = aF_{fy} - bF_{ry}, \quad (4.11)$$

In the case of a front-wheel drive (FWD) or all-wheel drive (AWD), additional right-hand-side terms appear in (4.10) and (4.11); however, these additional terms are usually considered small and are thus neglected.³

When the vehicle accelerates, or brakes, there is a normal tyre load transfer between the front and rear axles. By balancing moments around the rear-wheel ground-contact point, and noting that the sum of the tyre down forces is equal to the weight of the vehicle, the front and rear normal loads (F_{fz} and F_{rz} respectively) can be computed as:

$$F_{rz} = mg \frac{a}{a+b} + ma_x \frac{h}{a+b} \quad (4.12)$$

$$F_{fz} = mg - F_{rz}, \quad (4.13)$$

where h is the mass centre's height and a_x is the longitudinal acceleration, for small angles $a_x \approx \hat{a}_x$.

We will model the tyre forces using a simple slip-based model of the type alluded to in the introduction to this section. The lateral forces generated by the tyres are assumed to depend linearly on the tyre normal loads and slip angles, and are computed using

$$F_{fy} = C_{f0} F_{fz} \left(\delta - \frac{\omega a + v}{u} \right), \quad (4.14)$$

$$F_{ry} = C_{r0} F_{rz} \left(\frac{\omega b - v}{u} \right), \quad (4.15)$$

where C_{f0} and C_{r0} are the normalized cornering stiffnesses (at the front and rear axles respectively), which can be estimated from the (front and rear) tyre properties using C_α^{Fy}/F_z (with C_α^{Fy} given by (3.47) under brush model assumptions and given by (3.154) under string model assumptions), or using $B_y C_y D_y / F_z$ (with B_y, C_y, D_y being the Pacejka's coefficients introduced in Section 3.5.1); the small angle approximations (4.8) and (4.9) are used.

The tyre model (4.14)–(4.15) is combined with the remaining EOMs (4.10)–(4.11), and the resulting linear EOMs are given by:

$$\dot{v} = -\frac{C}{mu} v + \left(\frac{-C\nu}{mu} - u \right) \omega + \frac{C_f}{m} \delta, \quad (4.16)$$

$$\dot{\omega} = \frac{-C\nu}{mk^2 u} v - \frac{Cq^2}{mk^2 u} \omega + \frac{C_f a}{mk^2} \delta, \quad (4.17)$$

in which

³ In the case of FWD (4.1) gives (under small angle assumption) $F_{fx} = m(\dot{u} - \omega v) + F_{fy}\delta$, and the related $F_{fx}\delta$ and $aF_{fx}\delta$ terms in (4.10) and (4.11) are given in terms of this expression.

$$C_r = C_{r0}F_{rz} \quad (4.18)$$

$$C_f = C_{f0}F_{fz} \quad (4.19)$$

$$C\nu = C_fa - C_rb \quad (4.20)$$

$$C = C_f + C_r \quad (4.21)$$

$$Cq^2 = C_fa^2 + C_rb^2 \quad (4.22)$$

$$mk^2 = J. \quad (4.23)$$

This system represents a linear-time-invariant (LTI) model when the speed u is fixed, and a linear-time-varying (LTV) model in the case that u is varying. Following [8], the parameter ν is the distance between the centre of mass and the neutral steer point, q is the average moment arm, and k the radius of gyration. The neutral steer point, which is shown in Figure 4.1, has kinematic significance: a force applied through this point will cause the vehicle to move laterally without yawing.⁴

4.2.1 Constant speed case

When $u = u_0$, where u_0 is the steady-state velocity of the vehicle, (4.16) and (4.17) are time-invariant. In order to examine the car's behaviour, the response in the lateral acceleration, yaw velocity, and side-slip angle to perturbations in steering angle are determined. These quantities are given by the output response $\mathbf{y} = [\hat{a}_y, \omega, \beta]^T$, where the lateral acceleration is given by:

$$\hat{a}_y = \dot{v} + u_0\omega. \quad (4.24)$$

Here ω is a state, and β is given in (4.7).

The state-space model of the car from the steering angle δ to the output vector is given by⁵

$$\begin{aligned} A &= \begin{bmatrix} -\frac{C}{mu_0} & \frac{-C\nu}{mu_0} - u_0 \\ \frac{-C\nu}{Ju_0} & -\frac{Cq^2}{Ju_0} \end{bmatrix} & B &= \begin{bmatrix} \frac{C_f}{\frac{m}{aC_f}} \\ \frac{C_r}{J} \end{bmatrix} & \mathbf{x} &= \begin{bmatrix} v \\ \omega \end{bmatrix} \\ C &= \begin{bmatrix} -\frac{C}{mu_0} & -\frac{C\nu}{mu_0} \\ 0 & 1 \\ \frac{1}{u_0} & 0 \end{bmatrix} & D &= \begin{bmatrix} \frac{C_f}{m} \\ 0 \\ 0 \end{bmatrix}. \end{aligned} \quad (4.26)$$

⁴ The expression of the neutral steer point is obtained adding an external lateral force F_e in (4.16) together with the related external moment νF_e in (4.17) and solving for F_e and ν under the assumption of $\dot{v} = \dot{\omega} = \omega = \delta = 0$. A closely related concept is the *static margin*, which is defined as $-\nu/l$.

⁵ In the case that tyre relaxation is included ($\frac{\sigma_i}{u}\dot{F}_{iy} + F_{iy} = C_i\alpha_i$, where $i = f, r$, and σ is the relaxation length; see Chapter 3), the state and input matrices become

$$\begin{aligned} A &= \begin{bmatrix} 0 & -u & \frac{1}{m} & \frac{1}{m} \\ 0 & 0 & \frac{a}{J} & -\frac{b}{J} \\ -\frac{C_f}{\sigma_f} & -\frac{C_fa}{\sigma_f} & -\frac{\sigma_f}{u} & 0 \\ -\frac{C_r}{\sigma_r} & \frac{C_rb}{\sigma_r} & 0 & -\frac{u}{\sigma_r} \end{bmatrix} & B &= \begin{bmatrix} 0 \\ 0 \\ \frac{C_fu}{\sigma_f} \\ 0 \end{bmatrix} & \mathbf{x} &= \begin{bmatrix} v \\ \omega \\ F_{fy} \\ F_{ry} \end{bmatrix} & \mathbf{u} &= [\delta]. \end{aligned} \quad (4.25)$$

Steering implications. Under ‘small angle’ cornering, the yaw rate, the turn radius of curvature $\mathcal{C} = 1/\mathcal{R}$, and the vehicle’s speed are related by $V\mathcal{C} = \omega$. This can be expressed in state-space form using $\mathcal{C} = C_C \mathbf{x}$ with output matrix

$$C_C = \begin{bmatrix} 0 & 1/V \end{bmatrix}. \quad (4.27)$$

It follows from (4.26) that the transfer function $g(s)$, with s the Laplace variable, between the steering angle and the path curvature is given by

$$g(s) = C_C(sI - A)^{-1}B. \quad (4.28)$$

Under steady-state conditions the path curvature is given by

$$\begin{aligned} \mathcal{C} &= -C_C A^{-1} B \delta_{ss} \\ &= \frac{\delta_{ss}/w}{1 + \frac{V^2}{gw} \cdot \frac{(bC_r - aC_f)mg}{wC_r C_f}} \\ &= \frac{\delta_{ss}/w}{1 + \frac{V^2}{wg} \zeta} \end{aligned} \quad (4.29)$$

in which

$$\zeta = \frac{(bC_r - aC_f)mg}{wC_r C_f} \quad (4.30)$$

is the *understeer coefficient* or *understeer gradient* [8].⁶ Equation (4.29) can be solved for δ_{ss} to yield

$$\delta_{ss} = \frac{w}{\mathcal{R}} + \frac{a_y}{g} \zeta, \quad (4.31)$$

in which $\mathcal{R} = 1/\mathcal{C}$ is the path radius of curvature and $a_y = V^2\mathcal{C}$ is the car’s lateral acceleration. It follows from (4.31) that when $\zeta = 0$, the steering angle is independent of speed; this case is usually referred to as *neutral steering*. When $\zeta > 0$ (i.e. $bC_r > aC_f$ and $\nu < 0$), the steering angle must increase in proportion to $\frac{a_y}{g}$ in order to maintain a constant path curvature. Vehicles with this property are referred to as *understeering*. In order to maintain a constant path curvature when $\zeta < 0$ (i.e. $bC_r < aC_f$ and $\nu > 0$), the steering angle must be decreased in proportion to $\frac{a_y}{g}$ and the vehicle is referred to as *oversteering*.

These concepts can also be interpreted in terms of the tyre slips (4.5) and (4.6):

$$\alpha_f - \alpha_r = \delta_{ss} - \frac{\omega(a+b)}{u} \rightarrow \delta_{ss} = \frac{w}{\mathcal{R}} + \alpha_f - \alpha_r \quad (4.32)$$

in which we suppose that $u \approx V$ and $\omega/V = 1/\mathcal{R}$. It follows that in a neutral vehicle $\alpha_f = \alpha_r$, in an understeering vehicle $\alpha_f > \alpha_r$, and in an oversteering vehicle $\alpha_f < \alpha_r$.

⁶ The understeer gradient can be written in terms of the tyre cornering stiffness per unit load: $\zeta = \frac{mgb}{w} \frac{1}{C_f} - \frac{mga}{w} \frac{1}{C_r} = \frac{F_{zf0}}{C_f} - \frac{F_{zr0}}{C_r} = \frac{1}{C_{f0}} - \frac{1}{C_{r0}}$, where F_{zr0} and F_{zf0} are the normal tyre loads at standstill and C_{r0} and C_{f0} are the cornering stiffnesses normalized by the standstill load.

Two distinctive velocities can be derived from (4.31). An oversteering car ($\zeta < 0$) has a *critical speed*⁷ V_{cr} where the steer changes sign ($\delta_{ss} = 0$):

$$V_{cr} = \sqrt{-\frac{wg}{\zeta}}. \quad (4.33)$$

An understeering car ($\zeta > 0$) has a *characteristic speed* V_{ch} , where the steer angle is twice the kinematic or Ackermann steer angle ($\delta_{ss} = 2w/\mathcal{R}$):

$$V_{ch} = \sqrt{\frac{wg}{\zeta}}. \quad (4.34)$$

A third velocity is the *tangential speed* V_{tg} , which is the speed at which the longitudinal axis of the car is tangential to the trajectory ($v_{ss} = 0$):

$$V_{tg} = \sqrt{\frac{C_r bw}{am}}. \quad (4.35)$$

For $V < V_{tg}$ ($v_{ss} > 0$) the car travels on a turn ‘nose out’, while for $V > V_{tg}$ ($v_{ss} < 0$) the car travels ‘nose in’.⁸

The above analysis holds only for small slip angles (a linear model). A more general definition of the understeer coefficient, which is valid for large slip angles, is

$$\zeta = \frac{\partial}{\partial(a_y/g)} \left(\delta_{ss} - \frac{w}{\mathcal{R}} \right), \quad (4.36)$$

which is identical to (4.30) in the linear case. Furthermore, the understeering/oversteering behaviour (i.e. the sign of ζ) can be deduced from the sign of the even simpler expression

$$\left. \frac{\partial \delta_{ss}}{\partial V} \right|_{\mathcal{R}=\text{const}}, \quad (4.37)$$

which deals with rates of change rather than absolute quantities. As a consequence, a car may start understeering at small slips, which implies (4.37) > 0 and $\alpha_f > \alpha_r$, then at large slips become oversteering, that is, (4.37) < 0 , although $\alpha_f > \alpha_r$ hold true. This change of behaviour is related mainly to tyre nonlinearity.

These results have an interesting geometric interpretation that we now consider. The neutrally steering situation in which $\alpha_r = \alpha_f = \alpha$ is illustrated in Figure 4.2. Consider first that case in which the tyres are in pure non-slip rolling so that $\alpha_r = \alpha_f = 0$. In this case the lines connecting point C to the two tyre contact points are at right angles to the two wheel planes. If the front and rear tyres now operate with the same side slip angle, the instantaneous centre of rotation moves around the circumference of a circle as shown in Figure 4.2; this follows from the inscribed angle theorem. In this case the centre of rotation moves from C to C' as a result of tyre slip.

⁷ This speed is ‘critical’ because above it the car is unstable.

⁸ Under nose out conditions the projection of the velocity centre C falls behind the centre of mass G , while in nose-in conditions the projection of C falls ahead of G .

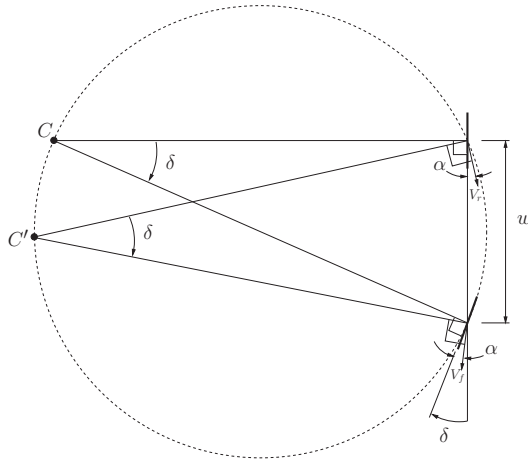


Figure 4.2: Neutral-steering single-track car model in which δ is the steering angle. The front- and rear-wheel tyre-contact velocity vectors are given by V_f and V_r respectively, with their corresponding side-slip angles given by α .

For any number of reasons the front- and rear-tyre side-slip angles may differ. Since the instantaneous centre of rotation is at the point of intersection of perpendiculars to the front- and rear-wheel velocity vectors, the centre of rotation moves from C' (as in Figure 4.2) to C'' (Figure 4.3) as the front-tyre slip angle reduces so that $\alpha_r > \alpha_f$, thereby producing an oversteering car. In order to maintain a constant-radius turn it follows from (4.31) that the steering angle has to be reduced as the vehicle's speed increases.

In an understeering car the tyre slip angles satisfy $\alpha_f > \alpha_r$ as shown in Figure 4.4. In this case the centre of rotation moves from C' (as in Figure 4.2) to C'' (Figure 4.4) as the front-tyre slip angle increases so that $\alpha_f > \alpha_r$. In order to hold a constant-radius turn in an understeering car, it follows from (4.31) that the steering angle has to be increased as the vehicle's speed increases.

Stability implications. The stability of this constant-velocity model has been studied extensively, for example in [8]. The poles of the system, which determine the car's stability, are the roots of the characteristic polynomial $\det(sI - A)$ with A given by (4.26). This gives

$$\lambda^2 + \frac{(a^2 + k^2)C_f + (b^2 + k^2)C_r}{mk^2u_0}\lambda + \left(\frac{w^2C_fC_r}{m^2k^2u_0^2} - \frac{C\nu}{mk^2}\right) = 0. \quad (4.38)$$

Following the Routh–Hurwitz criterion, the system will be stable if all the coefficients in (4.38) are positive. It is consequently clear that only an oversteering car can become unstable, since instability requires a positive value of $C\nu$ if the last term in (4.38) is to become negative. This occurs when the speed exceeds the critical value given by

$$u_0 > V_{crit} = \sqrt{\frac{w^2C_fC_r}{mC\nu}}. \quad (4.39)$$

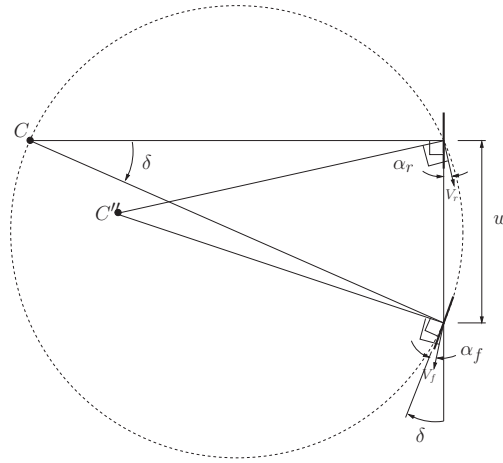


Figure 4.3: Oversteering single-track vehicle model. The front- and rear-wheel velocity vectors are given by V_f and V_r , with their corresponding side-slip angles satisfying $\alpha_r > \alpha_f$.

This is precisely the speed at which $\delta_{ss} = 0$, as derived above in (4.33).

To illustrate some of these ideas we consider a car with parameters given in Table 4.1. Two tyre sets have been chosen, in order to produce an understeering vehicle and an oversteering vehicle with a critical speed $V_{crit} \approx 70$ m/s.

From the state-space model in (4.26) the transfer functions from the steering angle to each of the outputs are determined. While the system poles are determined by the characteristic equation, the zeros of each of the three transfer functions are given by

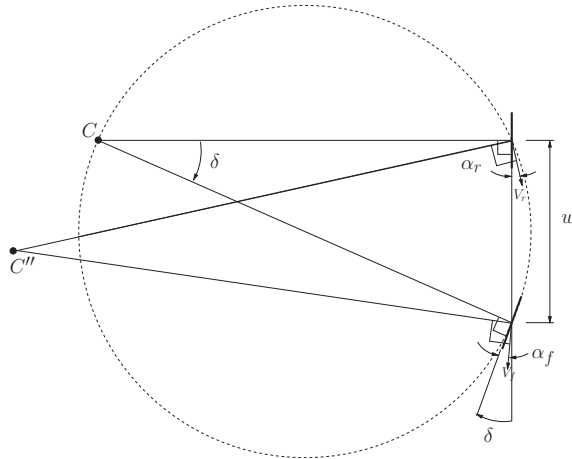


Figure 4.4: Understeering single-track vehicle, with the front- and rear-wheel side-slip angles satisfying $\alpha_F > \alpha_R$.

Table 4.1 Vehicle parameters.

Symbol	Description	Value
m	Car mass	720 kg
J	Moment of inertia about the z -axis	450 kg m ²
w	Wheelbase	3.4 m
a	Distance of mass centre from front axle	1.8 m
b	Distance of mass centre from rear axle	1.6 m
C_{f0}	Normalized front-tyre cornering stiffness (understeering)	25 rad ⁻¹
C_{r0}	Normalized rear-tyre cornering stiffness (understeering)	30 rad ⁻¹
C_{f0}	Normalized front-tyre cornering stiffness (oversteering)	30 rad ⁻¹
C_{r0}	Normalized rear-tyre cornering stiffness (oversteering)	25 rad ⁻¹

$$\{z_{a_y1}, z_{a_y2}\} = -\frac{bC_rw}{2Ju_0} \pm \sqrt{\left(\frac{bC_rw}{2Ju_0}\right)^2 - \frac{C_rw}{J}} \quad (4.40)$$

$$z_\beta = \frac{amu_0^2 - bC_rw}{Ju_0} \quad (4.41)$$

$$z_\omega = -\frac{C_rw}{mu_0a}. \quad (4.42)$$

The zeros z_{a_y} of the lateral acceleration transfer function will either be negative real, or will form a complex conjugate pair with a negative real part. The zero z_ω of the yaw velocity response transfer function will always be negative. At higher speeds, the zero z_β of the side-slip angle transfer function may become positive, resulting in a non-minimum phase response.

Figure 4.5 (a) shows the speed-dependent pole locations for the car with the parameters given in Table 4.1 and the understeering tyre combination. Both poles are non-oscillatory at low speed. As the speed increases, the poles move together along the

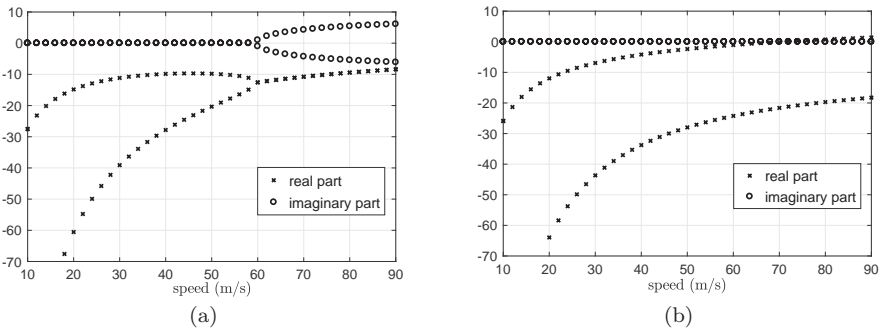


Figure 4.5: Real and imaginary parts of the simple car model eigenvalues for the parameters given in Table 4.1; (a) the understeering car, and (b) the oversteering car.

negative real axis, coalescing at 60 m/s into an oscillatory complex-conjugate pair. The oscillatory frequency then increases with speed and the poles move towards the right-half plane. The case of the oversteering tyre combination is shown in Figure 4.5 (b); the poles are again non-oscillatory at low speed. As the speed increases, the poles migrate towards the right-half plane. At the critical speed (4.39) of ≈ 70 m/s one pole enters the right-half plane, indicating instability. The tangential speeds (4.35) are 22 m/s and 20 m/s for the understeering and oversteering car respectively.

4.2.2 Accelerating and braking

It is shown in [160] that the vehicle model given in (4.26) can be considered slowly time-varying and therefore that the eigenvalues can be used to assess the vehicle's stability. As the vehicle accelerates (or decelerates), the frozen-time eigenvalues evolve with time and can be used to assess the time-localized stability of the car. These results are compared with the closed-form solution of the describing time-varying linear differential equation.

Closed-form solution. The first-order differential equations (4.16) and (4.17) can be combined by eliminating the lateral velocity to produce a second-order differential equation in the yaw rate ω . The analysis is further simplified by assuming that the steering angle is held at zero in order to obtain

$$u(t)^2 \ddot{\omega} + Pu(t)\dot{\omega} + (Qu(t)^2 + R)\omega = 0, \quad (4.43)$$

where the parameters P , Q , and R are given by

$$P = \frac{-k^2 ma_x + (a^2 + k^2)C_f + (b^2 + k^2)C_r}{mk^2}, \quad Q = -\frac{C\nu}{mk^2}, \quad R = \frac{w^2 C_f C_r}{m^2 k^2}. \quad (4.44)$$

This time-varying differential equation has a structure reminiscent of a Bessel's differential equation, and a closed-form solution can be found in terms of Bessel functions. As demonstrated in [161], an equation with the form

$$u^2 \frac{d^2 \omega}{du^2} + Pu \frac{d\omega}{du} + (Qu^2 + R)\omega = 0 \quad (4.45)$$

has solution

$$\omega = c_1 u^\rho(t) J_\nu(\alpha u(t)) + c_2 u^\rho(t) Y_\nu(\alpha u(t)), \quad (4.46)$$

in which J_ν and Y_ν are Bessel functions of the first and second kind, with c_1 and c_2 constants of integration. To convert (4.43) into (4.45), a change in the independent variable from t to u is required. The first- and second-order derivatives of ω with respect to u are

$$\frac{d\omega}{dt} = \frac{d\omega}{du} \frac{du}{dt} = a_x \frac{d\omega}{du} \quad (4.47)$$

and

$$\frac{d^2 \omega}{dt^2} = \frac{d^2 \omega}{du^2} \left(\frac{du}{dt} \right)^2 + \frac{d\omega}{du} \frac{d^2 u}{dt^2} = a_x^2 \frac{d^2 \omega}{du^2} \quad (4.48)$$

since the acceleration is assumed constant. The parameters ρ and α , and the order of the Bessel functions ν , can now be related to the coefficients of the differential equation and a_x by:

$$\rho = \frac{1 - \frac{P}{a_x}}{2}, \quad \alpha = \sqrt{\frac{Q}{a_x^2}}, \quad \nu = \sqrt{\frac{(1 - \frac{P}{a_x})^2}{4} - \frac{R}{a_x^2}}. \quad (4.49)$$

If Q is negative, the argument of the Bessel functions is complex. In this case, in order to obtain real solutions, modified Bessel functions I_ν and K_ν of the first and second kind must be used to obtain

$$\omega = c_1 u^\rho(t) I_\nu(\alpha u(t)) + c_2 u^\rho(t) K_\nu(\alpha u(t)). \quad (4.50)$$

The sign of Q is determined by the sign of $C\nu$ (4.20). However, unlike the constant-velocity case, this quantity is a function of the vehicle acceleration. A car might be oversteering at a constant velocity ($C\nu > 0$), but when the vehicle accelerates, the normal load transfer to the rear increases C_r and reduces simultaneously C_f , which may cause the car to understeer ($C\nu < 0$). Under braking the opposite occurs and $C\nu$ may remain positive (or it may become positive if the vehicle was initially understeering). As the sign of $C\nu$ changes, the sign-appropriate Bessel functions must be used.

If the velocity is assumed constant the yaw differential equation reduces to a linear second-order time-invariant equation with solution

$$\omega = c_1 e^{\lambda_1 t} + c_2 e^{\lambda_2 t}, \quad (4.51)$$

where λ_1 and λ_2 are real eigenvalues. The constants c_1 and c_2 , once again, come from initial conditions. When $C\nu$ is negative (understeering), and the speed sufficiently high, the eigenvalues may become complex. The time-invariant yaw response will differ from the time-varying solution over long time periods, and short-horizon time-invariant yaw responses must be pieced together. Suppose that the time horizon is divided into a sequence of subintervals, and that the time-invariant solution is computed on each subinterval with the terminal conditions from the previous interval used as the initial conditions for the current interval. As these subintervals decrease in duration the solution accuracy, as expected, improves.

The eigenvalues and system responses for constant $\pm 10 \text{ m/s}^2$ of acceleration/braking are shown in Figure 4.6 for the car parameters given in Table 4.1, with the oversteering tyre combination, and for an initial yaw velocity of 0.001 rad/s . When braking from 80 m/s to 20 m/s , one of the frozen-time eigenvalues changes sign at $V_{crit} \approx 40 \text{ m/s}$, which is much lower than the 70 m/s found for the constant-velocity case. The load transfer due to braking reduces the rear-tyre cornering stiffness, while increasing that in the front. This, in turn, leads to an accompanying reduction in the critical speed; see (4.39). The response of the time-varying system to a non-zero initial yaw velocity at 80 m/s is determined using the closed-form solution in (4.46). Initially, the yaw angle grows exponentially, typical of an unstable system. However, as the vehicle speed decreases, and the eigenvalues become negative, the yaw angle response slows and then

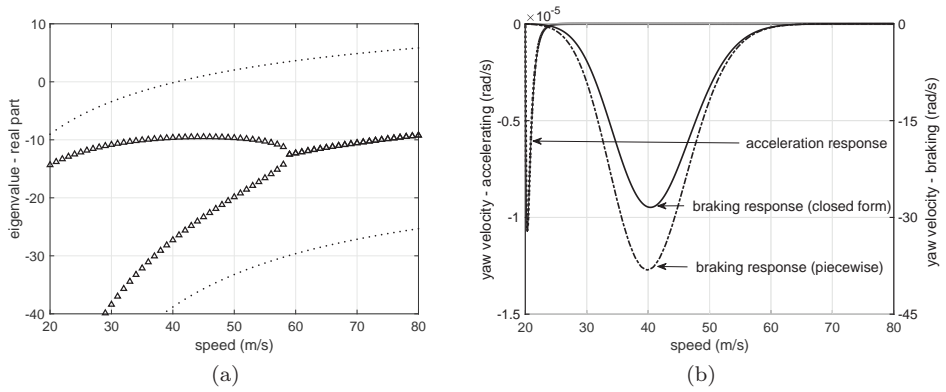


Figure 4.6: (a) shows the real parts of the frozen-time eigenvalues of a vehicle accelerating in straight running at 10 m/s^2 from 20 m/s to 80 m/s (shown as the curve formed from \triangle s), and a vehicle braking in straight running at -10 m/s^2 for vehicle speeds from 80 m/s to 20 m/s (shown dotted). (b) shows the yaw response to a non-zero initial yaw velocity at 20 m/s for the accelerating case, and at 80 m/s for braking.

decays. This behaviour suggests that a vehicle braking from 80 m/s may exhibit an undesirable ‘burst’ response in the 40 m/s speed range. Under acceleration the oversteering vehicle becomes understeering and the system response is stable. At higher speeds the eigenvalues are complex, which manifests in an underdamped yaw response to a perturbation.

4.2.3 Cornering

The straight-running analysis can be extended to the cornering case for both constant and variable speeds, but this must be done with care.

Constant-velocity case. The first complication relates to the fact that under cornering conditions the longitudinal and lateral dynamics given in (4.1) and (4.2) interact. The second complication relates to the fact that in cornering, the steady-state tyre side-slip angles are no longer zero and the linear tyre model given in (4.15) is not reasonably usable, unless the lateral accelerations are small. In these cases more complex tyre models of the form

$$F_y = f(\alpha, \kappa, F_z) \quad (4.52)$$

should be employed (see (3.84) and (3.109)–(3.110)); α , κ , and F_z are respectively the side-slip angle, the longitudinal slip, and the normal load. For present purposes we treat the tyre force laws as nonlinear functions of the three argument variables.

If the EOMs in (4.1), (4.2), and (4.3) are linearized about a constant speed and a constant steady-state radius-of-turn, one obtains:

$$\begin{aligned}
A &= \begin{bmatrix} \frac{-C_f \delta_0 (v_0 + a \omega_0)}{m u_0^2} & \frac{C_f \delta_0}{m u_0} + \omega_0 & \frac{C_f a \delta_0}{m u_0} + v_0 \\ \frac{C v_0 + C s \omega_0}{m u_0^2} - \omega_0 & -\frac{C}{m u_0} & -\frac{C s}{m u_0} - u_0 \\ \frac{C s v_0 + C q^2 \omega_0}{J u_0^2} & -\frac{C s}{J u_0} & -\frac{C q^2}{J u_0} \end{bmatrix} & B &= \begin{bmatrix} \frac{-C_f \delta_0 + F_{fy0}}{m} \\ \frac{C_f - F_{fy0} \delta_0}{J} \\ \frac{C_f a - F_{fy0} a \delta_0}{J} \end{bmatrix} \\
C &= \begin{bmatrix} \frac{C s \omega_0 + v_0 C}{m u_0^2} & -\frac{C}{m u_0} & -\frac{C s}{m u_0} \\ 0 & 0 & 1 \\ -\frac{v_0}{u_0} & \frac{1}{u_0} & 0 \end{bmatrix} & D &= \begin{bmatrix} \frac{C_f - F_{fy0} \delta_0}{m} \\ 0 \\ 0 \end{bmatrix}.
\end{aligned} \tag{4.53}$$

The outputs are again $[\hat{a}_y, \delta, \omega]$. For the front tyre one has

$$\begin{bmatrix} \frac{\partial F_{fy}}{\partial u} \\ \frac{\partial F_{fy}}{\partial v} \\ \frac{\partial F_{fy}}{\partial \omega} \\ \frac{\partial F_{fy}}{\partial \delta} \end{bmatrix} = \frac{\partial F_{fy}}{\partial \alpha_f} \bigg|_{\alpha_{f0}, \kappa_{f0}, F_{fz0}} \begin{bmatrix} \frac{\partial \alpha_f}{\partial u} \\ \frac{\partial \alpha_f}{\partial v} \\ \frac{\partial \alpha_f}{\partial \omega} \\ \frac{\partial \alpha_f}{\partial \delta} \end{bmatrix}_{u_0, v_0, \omega_0, \delta_0} = C_f \begin{bmatrix} \frac{\omega_0 a + v}{u^2} \\ -\frac{1}{u_0} \\ -\frac{a}{u_0} \\ 1 \end{bmatrix}, \tag{4.54}$$

in which C_f is the gradient of the tyre force characteristic local to the steady-state operating point; C_f is operating point dependent. For the rear tyre one has

$$\begin{bmatrix} \frac{\partial F_{ry}}{\partial u} \\ \frac{\partial F_{ry}}{\partial v} \\ \frac{\partial F_{ry}}{\partial \omega} \\ \frac{\partial F_{ry}}{\partial \delta} \end{bmatrix} = \frac{\partial F_{ry}}{\partial \alpha_r} \bigg|_{\alpha_{r0}, \kappa_{r0}, F_{rz0}} \begin{bmatrix} \frac{\partial \alpha_r}{\partial u} \\ \frac{\partial \alpha_r}{\partial v} \\ \frac{\partial \alpha_r}{\partial \omega} \\ \frac{\partial \alpha_r}{\partial \delta} \end{bmatrix}_{u_0, v_0, \omega_0, \delta_0} = C_r \begin{bmatrix} \frac{v - \omega_0 b}{u^2} \\ -\frac{1}{u_0} \\ -\frac{b}{u_0} \\ 0 \end{bmatrix}. \tag{4.55}$$

The operating conditions required to evaluate the linearized model are determined by the steady-state speed V and turn radius \mathcal{R} . Once V and \mathcal{R} have been chosen, ω is determined by the kinematic relation:

$$\omega = \frac{V}{\mathcal{R}}. \tag{4.56}$$

The resultant vehicle speed is related to the lateral and longitudinal velocity magnitudes by

$$V^2 = v^2 + u^2. \tag{4.57}$$

Under steady-state conditions, the EOMs reduce to the following algebraic relations (for a RWD car)

$$0 = m \omega_0 v_0 - F_{fy0} \delta_0 + F_{rx0} \tag{4.58}$$

$$0 = -m \omega_0 u_0 + F_{fy0} \cos \delta_0 + F_{ry0} \tag{4.59}$$

$$0 = a F_{fy0} \cos \delta_0 - b F_{ry0}. \tag{4.60}$$

These five equations and the two nonlinear tyre models can be solved simultaneously to determine the steady-state values of u_0 , v_0 , ω_0 , δ_0 , as well as F_{rx0} , which is the (small) driving force required to maintain the vehicle at a constant velocity. This steady-state solution, together with the local tyre stiffnesses C_f and C_r , can now be substituted in (4.53) in order to determine the local steering dynamics and stability of the car.

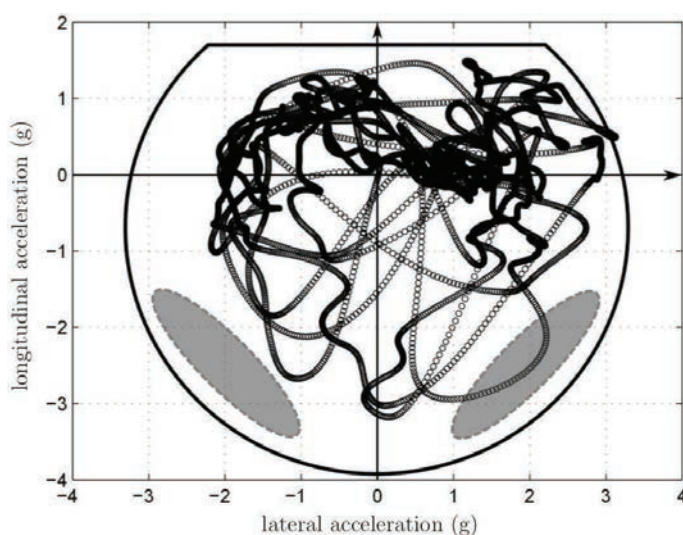


Figure 4.7: Sample G-G diagram of a Formula One car that shows the vehicle's lateral and longitudinal acceleration on a qualifying lap at Silverstone. The track contains eighteen corners, of which ten are right-handed; this accounts for the vehicle's positive-dominated lateral acceleration. In addition, the high-speed corners, out of which the driver accelerates, are also right-handed, which is consistent with vehicle's prolonged operation in the top-right quadrant of the diagram.

Acceleration and braking under cornering. The operating characteristics of cars are often described in terms of a so-called G-G diagram (Figure 4.7). In this diagram the lateral acceleration of the vehicle is plotted against the longitudinal acceleration with a boundary representing the physical limits of the car. The engine power is the primary influence on the positive longitudinal acceleration limit, while the tyre grip is the key factor in determining the lateral and braking limits. A graphical overlay of recorded telemetry data can be used to analyse the driver's exploitation of the performance envelope. In racing, the more the driver is able to utilize the capability of the vehicle, the lower the lap time.

Handling and stability characteristics influence the driver's ability to operate the vehicle on the limit of performance. An unstable vehicle may undermine the driver's confidence, or in extreme cases make the vehicle undrivable. The highlighted regions in Figure 4.7 correspond to areas in which the vehicle is typically unstable and more difficult to control, thus requiring highly skilled drivers. Characterizing the vehicle stability across the G-G diagram is useful for predicting the extent to which the driver is able to exploit the vehicle's performance. The treatment of stability over the full operating range of the vehicle has produced a number of analysis techniques, but all have their limitations [162–164]

Straight-line accelerating and braking, and steady-state cornering, only represent the axes of the G-G diagram. To determine the stability over the rest of the operating

regime it is necessary to develop a method of examining acceleration and braking under cornering. In this scenario, the vehicle is no longer in equilibrium, since the states are changing with time. It is possible to study the stability of an accelerating or braking vehicle by examining perturbations from some nominal motion [165]. To conduct this type of analysis the vehicle states along a nominal prescribed trajectory are required. These evolving states can be found by simulating the manoeuvre using the nonlinear vehicle model with feedback controllers that are used to generate the plant inputs that produce the required motion. This approach has a number of limitations: simulating the manoeuvre is a time-consuming process and determining vehicle stability is intended to be a way predicting the vehicle's response *without having to numerically integrate the equations of motion!* Furthermore, as the vehicle becomes unstable, and the braking and acceleration become more aggressive, the feedback controllers are less able to maintain the vehicle on the reference trajectory.

An alternative approach to determining the frozen-time vehicle states is to use a d'Alembert force system that acts as a surrogate for the real forces of inertia experienced under acceleration. In this approach, an accelerating or braking vehicle is approximated by one travelling at a constant velocity, but subjected to forces that capture the inertial effects of accelerating and braking. The advantage of this method is clear. The vehicle remains in equilibrium and the vehicle states can be determined from algebraic equations of motion, which now contain additional terms representing the apparent forces. The frozen-time eigenvalues of the system are computed at each point along a motion trajectory. The choice of manoeuvres used to 'fill out' the G-G diagram is not unique [166].

4.3 Timoshenko–Young bicycle

4.3.1 Introduction

The next introductory example is a simple bicycle model analysis due to Timoshenko and Young [167]; see Figure 4.8. The coordinates of the rear-wheel ground-contact point are (x, y) and are given in an inertial reference frame $Oxyz$. The vehicle's roll angle is ϕ and its yaw angle is ψ . The steer angle δ is measured between the front frame and the rear frame. The vehicle's mass m is concentrated at its mass centre that is a distance h from the line joining the two wheel ground-contact points, and a distance b in front of the rear-wheel ground-contact point. The acceleration due to gravity is denoted g , which points in the positive z -direction. The machine's wheelbase is w . Although wheels are drawn in Figure 4.8, they are both massless and inertia-less and so can be conceptually replaced by skates that can only slip in the direction in which they point (much like the Čaplygin sleigh; see Section 2.8). To make the analysis easier, we assume that the radius of the front wheel is vanishingly small and that consequently the front-wheel ground-contact point is independent of the roll and steer angles.

4.3.2 Steering kinematics

The motion of the bicycle's wheels (skates) are constrained by a pure rolling assumption. Under this assumption the rear wheel must move in the direction of its line of

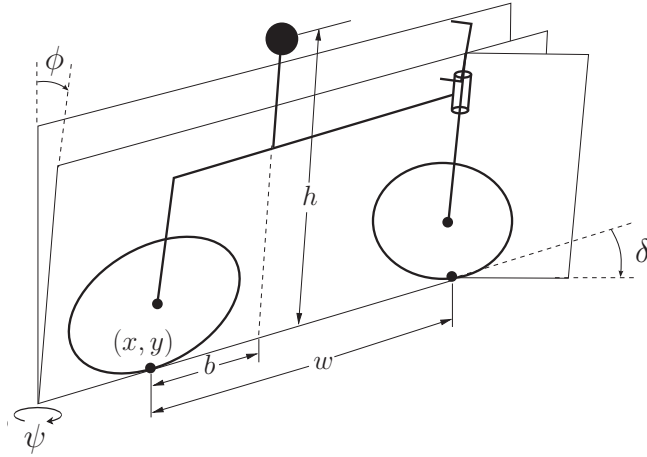


Figure 4.8: Timoshenko–Young bicycle. The yaw angle is denoted by ψ , the roll angle by ϕ , and the steer angle by δ . The mass centre is located at $(x + b, y - h)$ when the bicycle is upright and aligned with the positive x -axis. The wheelbase is w .

intersection with the ground plane. Thus

$$\dot{x} = uc_\psi \quad (4.61)$$

$$\dot{y} = us_\psi, \quad (4.62)$$

in which u is the vehicle's forward speed as measured at the rear ground-contact point, and s_ψ and c_ψ represent the sine and cosine of ψ . There are rolling constraints associated with the front wheel too.

Referring to Figure 4.9 we see that the bicycle's mass is located at

$$x_G = x + bc_\psi - hs_\psi s_\phi \quad (4.63)$$

$$y_G = y + bs_\psi + hc_\psi s_\phi \quad (4.64)$$

$$z_G = -hc_\phi, \quad (4.65)$$

while the front-wheel ground-contact point is located at

$$x^{fw} = x + wc_\psi \quad (4.66)$$

$$y^{fw} = y + ws_\psi. \quad (4.67)$$

The front-wheel ground-contact point velocity is thus

$$\dot{x}^{fw} = uc_\psi - w\dot{\psi}s_\psi \quad (4.68)$$

$$\dot{y}^{fw} = us_\psi + w\dot{\psi}c_\psi \quad (4.69)$$

in which (4.61) and (4.62) were used.

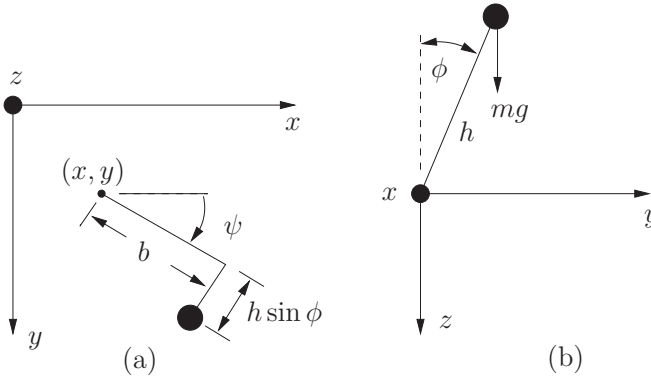


Figure 4.9: Timoshenko–Young bicycle. In Figure (a) the z -axis points into the page, while in Figure (b) the x -axis points into the page.

The bicycle's orientation in the inertial reference frame can be found using

$$\mathcal{R}_I = \mathcal{R}(\mathbf{e}_z, \psi) \mathcal{R}(\mathbf{e}_x, \phi) = \begin{bmatrix} c_\psi & -s_\psi c_\phi & s_\psi s_\phi \\ s_\psi & c_\psi c_\phi & -c_\psi s_\phi \\ 0 & s_\phi & c_\phi \end{bmatrix}. \quad (4.70)$$

The steering behaviour can be computed using

$$\mathcal{R}_S = \begin{bmatrix} c_\delta & -s_\delta & 0 \\ s_\delta & c_\delta & 0 \\ 0 & 0 & 1 \end{bmatrix}, \quad (4.71)$$

in which δ is the steering angle. If $\boldsymbol{\lambda}_B^{fw} = [0 \ 1 \ 0]^T$ is a unit vector aligned with the front wheel spindle in body-fixed coordinates, then

$$\boldsymbol{\lambda}_I^{fw} = \mathcal{R}_I \mathcal{R}_S \boldsymbol{\lambda}_B^{fw} \quad (4.72)$$

$$= \begin{bmatrix} -c_\psi s_\delta - s_\psi c_\phi c_\delta \\ -s_\psi s_\delta + c_\psi c_\phi c_\delta \\ s_\phi c_\delta \end{bmatrix} \quad (4.73)$$

is in the inertial reference frame. The projection of this vector onto the ground plane is orthogonal to the line of intersection between the front wheel and the ground plane. We call this vector \mathbf{n} :

$$\mathbf{n} = \begin{bmatrix} -c_\psi s_\delta - s_\psi c_\phi c_\delta \\ -s_\psi s_\delta + c_\psi c_\phi c_\delta \\ 0 \end{bmatrix}. \quad (4.74)$$

Under pure rolling the front wheel's ground-contact point velocity must follow the line of intersection between the wheel and the ground plane. Since the ground-contact

point velocity and \mathbf{n} must be orthogonal, there holds $[\dot{x}^{fw}, \dot{y}^{fw}, 0]^T \cdot \mathbf{n} = 0$, which gives

$$\dot{\psi} = \frac{vt_\delta}{wc_\phi}, \quad (4.75)$$

in which t_δ is $\tan \delta$. This equation shows how the yaw rate, and thus the radius of turn, is dictated (kinematically) by the steering angle.

We conclude this section by introducing the kinematic steering angle Δ for the Timoshenko–Young bicycle. Under the assumptions associated with nonholonomic rolling, the wheels must travel in the direction of the lines of intersection of the wheel planes and the ground plane. The kinematic steering angle is the angle between these lines of intersection, and therefore the angle between the front- and rear-wheel velocity vectors. Without loss of generality the rear wheel may be instantaneously aligned with the x -axis by setting $\psi = 0$. That is

$$\Delta = \tan^{-1} \left(\frac{\dot{y}^{fw}}{\dot{x}^{fw}} \right) \bigg|_{\psi=0} = \tan^{-1} \left(\frac{t_\delta}{c_\phi} \right) \quad (4.76)$$

using (4.68), (4.69), and (4.75), where $t_\delta = \tan \delta$. The steering angle δ and the kinematic steering angle Δ are different when the bicycle is ‘leaned over’. Since the instantaneous radius of curvature $\hat{\mathcal{R}}$ and the yaw rate are related by

$$u = \dot{\psi} \hat{\mathcal{R}}, \quad (4.77)$$

it follows from (4.75) that the instantaneous radius of curvature is given by $\hat{\mathcal{R}} = \frac{wc_\phi}{t_\delta}$, with the path curvature given by

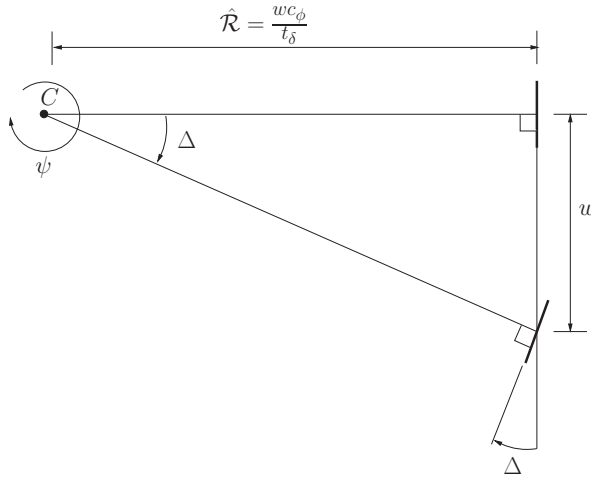


Figure 4.10: Ground-plane kinematics of the Timoshenko–Young model. The kinematic steering angle Δ is the angle between the line of intersection of the front wheel and the ground plane and the line of intersection of the rear wheel and the ground plane. The instantaneous centre of rotation is C .

$$\mathcal{C} = \frac{1}{\hat{\mathcal{R}}} = \frac{t_\delta}{wc_\phi}. \quad (4.78)$$

The ground-plane kinematics of the Timoshenko–Young bicycle are shown in Figure 4.10. It follows from (4.78) that the radius of turn will ‘tighten’ if the bicycle is rolled over at fixed steering angle. A detailed study of motorcycle steering kinematics can be found in chapter 1 of [6].

4.3.3 Vehicle dynamics

We will determine the vehicle’s equations of motion using Newton–Euler vector mechanics principles. To eliminate the reactions at the road–wheel contacts, we take moments around an axis that passes between the wheel ground-contact points. Without loss of generality we can consider an instant when the axis of moments is aligned with the x -axis. Taking moments gives

$$0 = gs_\phi - \ddot{z}_G s_\phi - \ddot{y}_G c_\phi. \quad (4.79)$$

It follows from (4.64) and (4.65) that

$$\ddot{y}_G|_{\psi=0} = u^2\mathcal{C} + b\ddot{\psi} - hs_\phi\dot{\phi}^2 + hc_\phi\ddot{\phi} - hs_\phi u^2\mathcal{C}^2 \quad (4.80)$$

$$\ddot{z}_G = hc_\phi\dot{\phi}^2 + hs_\phi\ddot{\phi}, \quad (4.81)$$

since

$$\dot{\psi} = u\mathcal{C}$$

and

$$\ddot{y}|_{\psi=0} = u^2\mathcal{C},$$

in which \mathcal{C} is the instantaneous curvature of the rear-wheel ground-contact point trajectory. Substitution into (4.79) gives

$$h\ddot{\phi} = gs_\phi - c_\phi \left((1 - h\mathcal{C}s_\phi)\mathcal{C}u^2 + b\ddot{\psi} \right). \quad (4.82)$$

An alternative version of (4.82), which is in terms of the steer angle rather than the yaw angle, can be obtained from (4.75) as

$$h\ddot{\phi} = gs_\phi - t_\delta \left(\frac{u^2}{w} + \frac{b\dot{u}}{w} + t_\phi \left(\frac{ub}{w}\dot{\phi} - \frac{hu^2}{w^2}t_\delta \right) \right) - \frac{bu\dot{\delta}}{wc_\phi^2}. \quad (4.83)$$

An inspection of either (4.82) or (4.83) shows that the Timoshenko–Young bicycle model is time-reversible and so is likely neutrally stable.

4.3.4 Lagrange’s equation

The bicycle’s kinetic energy is given by

$$T = \frac{m}{2}(\dot{x}_G^2(t) + \dot{y}_G^2(t) + \dot{z}_G^2(t)), \quad (4.84)$$

in which \dot{x}_G , \dot{y}_G , and \dot{z}_G can be computed using (4.63), (4.64), and (4.65). The machine's potential energy is

$$V = -mgz_G, \quad (4.85)$$

and so the Lagrangian is given by

$$\mathcal{L} = T - V. \quad (4.86)$$

If we solve

$$0 = \frac{d}{dt} \left(\frac{\partial \mathcal{L}}{\partial \dot{\phi}} \right) - \left(\frac{\partial \mathcal{L}}{\partial \phi} \right) \quad (4.87)$$

for $\ddot{\phi}$, and substitute for the accelerations \ddot{x}_G , \ddot{y}_G , and \ddot{z}_G that can be computed using (4.63), (4.64), and (4.65), then (4.82) again follows. Equation (4.83) can be found by substituting (4.75) as before.

As is explained in Section 2.2.8, any nonholonomic constraints are enforced by appending them to Lagrange's equations using Lagrange multipliers. In this case the time derivative of the roll coordinate does not appear in the constraint equations (4.68) and (4.69) and so the inclusion of Lagrange multipliers in (4.87) is unnecessary.

4.3.5 Linearized model

Equation (4.83) represents the nonholonomic Timoshenko–Young bicycle with control inputs δ and u . This equation can be linearized about a constant-speed straight-running condition in order to obtain a simple linear model that relates to small perturbation behaviour:

$$\ddot{\phi} = \frac{g}{h}\phi - \frac{u^2}{hw}\delta - \frac{bu}{wh}\dot{\delta}. \quad (4.88)$$

By taking Laplace transforms, we obtain from (4.88) the single-input single-output transfer function between δ and ϕ

$$H_{\phi\delta}(s) = -\frac{bu}{wh} \frac{s + u/b}{s^2 - g/h}, \quad (4.89)$$

which has a speed-dependent gain, a speed-dependent zero at $-u/b$, and fixed poles at $\pm\sqrt{g/h}$. The unstable pole corresponds to an inverted-pendulum-type capsizing mode. The zero is in the left-half plane under forward-running conditions. It then moves through the origin into the right-half plane as the speed is reduced to zero, and then reverses in sign. Under backward-running conditions the right-half plane zero, which for some speeds comes into close proximity to the right-half plane pole, is associated with the control difficulties found in rear-steering bicycles [168].

Equation (4.89) tells us that in straight running the linearized Timoshenko–Young bicycle is always unstable with a fixed pole at $\sqrt{g/h}$; this is reminiscent of the unstable capsizing mode associated with the simple inverted pendulum. This property does not carry over to even slightly more realistic models of the type considered in Section 4.4; in this case the poles of the linearized system become speed dependent and the vehicle model has a stable speed range. In more realistic models, certain of the vehicle's transfer functions have a right-half plane zero for positive speeds, resulting in a phenomenon known as 'counter steering'; more will be said about this in Chapter 5.

4.4 Lumped-mass bicycle

The ability of a bicycle to ‘self balance’ is one of its most important features. This self-stability property was not a feature of the Timoshenko–Young bicycle analysed in Section 4.3, and so the Timoshenko–Young model lacks at least one important dynamic feature of a practical bicycle. In order to begin the process of understanding this self-stability property, we will analyse briefly a point-mass bicycle introduced in [169] and illustrated in Figure 4.11. The key feature of this point-mass bicycle is that it is stable over a range of speed even though it has neither mechanical trail nor gyroscopic influences, which have for a long time been considered essential for a self-balancing two-wheeled vehicle. In broad terms, however, trail and gyroscopic moments are beneficial to stability.

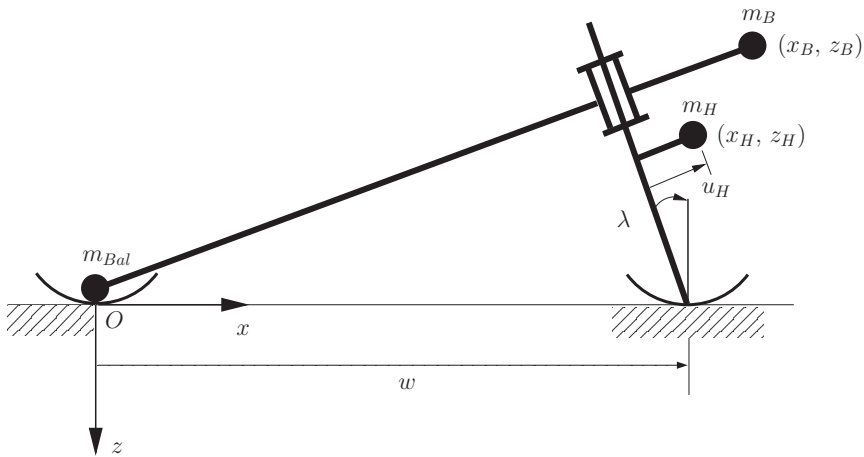


Figure 4.11: Primitive lumped-mass bicycle.

The primitive point-mass bicycle comprises three point masses, an inclined steering axis, and wheels without mass or inertia. From a dynamic modelling perspective the wheels may be treated as ‘skates’ that ensure that the vehicle proceeds along the lines of intersection between the ground plane and the two wheel planes. The rear frame has mass m_B and a ballast mass m_{Bal} , which is located at the rear-wheel ground-contact point. The ballast mass plays no role in the lateral dynamics, and serves only to prevent the rear wheel leaving the ground, thereby allowing the machine to pitch forward. The machine parameters we will use in this short study are given in Table 4.2.

4.4.1 Equations of motion

The first equation of motion comes from a momentum balance around an axis in the ground plane that is instantaneously aligned with the line of intersection between the rear frame and the ground plane:

$$T_B + g(u_H m_H \delta - (m_B z_B + m_H z_H) \varphi) = (m_B z_B^2 + m_H z_H^2) \ddot{\varphi} - (m_B z_B + m_H z_H) \ddot{y}_R - (m_B x_B z_B + m_H x_H z_H) \ddot{\psi} - m_H u_H z_H \ddot{\delta}, \quad (4.90)$$

where \ddot{y}_R is the lateral acceleration of the rear-wheel ground-contact point. The terms on the left-hand side include an external roll moment T_B , and gravitational terms relating to roll (φ) and steer influences (δ). The terms on the right of this equation relate respectively to the machine's roll acceleration, its lateral acceleration (\ddot{y}_R), its yaw acceleration, and the steering angle acceleration. The perpendicular distance between the front frame mass m_H and the steer axis is given by

$$u_H = (x_H - w) \cos \lambda - z_H \sin \lambda,$$

as can be confirmed by a simple geometric calculation.

The second equation comes from an angular momentum balance around the steering axis.

$$T_{HB} + g(\varphi + \delta \sin \lambda) m_H u_H = m_H u_H \ddot{y}_R - m_H u_H z_H \ddot{\varphi} + m_H u_H x_H \ddot{\psi} + m_H u_H^2 \ddot{\delta}. \quad (4.91)$$

The terms on the left-hand side of this equation contain forcing terms due to the steering moment T_{HB} and gravity-related roll and steer terms. The terms on the right-hand side of this equation describe the machine's lateral acceleration and inertial terms relating to roll, yaw, and steering respectively.

To obtain the equations that describe the bicycle's behaviour for small perturbations from straight running, we now need to recognize the nonholonomic constraints associated with the two road wheels (skates). The road-contact constraints allow the lateral position and its derivatives, and the yaw angle and its derivatives, to be expressed in terms of the steer angle. Figure 4.12 shows that the instantaneous radius of curvature is given by

$$\hat{R} = \frac{w}{\delta \cos \lambda},$$

in which $\delta \cos \lambda$ is the (small) kinematic steering angle, which is the angle between the line of intersection of the rear wheel and the ground plane and the line of intersection

Table 4.2 Lumped-mass bicycle parameters.

Parameters	Symbol	Value
Wheelbase	w	1.0 m
Steer axis tilt angle	λ	$5\pi/180$ rad
Gravity	g	9.81 m/s ²
Rear frame		
Position of centre of mass	(x_B, y_B, z_B)	(1.2, 0.0, -0.4) m
Mass	m_B	10 kg
Front frame		
Position of centre of mass	(x_H, y_H, z_H)	(1.02, 0.0, -0.2) m
Mass	m_H	1 kg

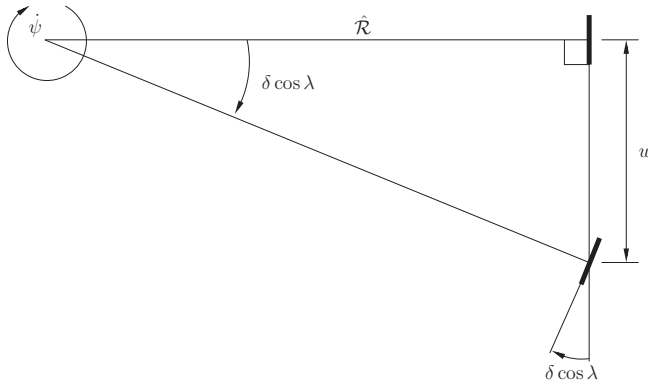


Figure 4.12: Bicycle ground-plane kinematics.

of the front wheel and the ground plane. For small angles, a handlebar steering angle of δ results in a kinematic steering angle of $\delta \cos \lambda$ and a (front-wheel) camber angle of $\delta \sin \lambda$. This means that the lateral acceleration \ddot{y}_R may be expressed as

$$\ddot{y}_R = \frac{u^2}{\hat{\mathcal{R}}} = \frac{u^2 \delta \cos \lambda}{w}, \quad (4.92)$$

where u is the velocity at the rear contact point. It is also clear that

$$\dot{\psi} = \frac{u}{\hat{\mathcal{R}}} = \frac{u \delta \cos \lambda}{w}$$

and so

$$\ddot{\psi} = \frac{u \dot{\delta} \cos \lambda}{w}.$$

The final roll equation comes from (4.90) and (4.91), once \ddot{y}_R and $\ddot{\psi}$ have been eliminated. The resulting equations can be written in the form

$$M\ddot{\mathbf{q}} + uC\dot{\mathbf{q}} + g(K_0 + u^2 K_2)\mathbf{q} = \begin{bmatrix} T_B \\ T_{HB} \end{bmatrix}, \quad (4.93)$$

in which $\mathbf{q} = [\phi, \delta]^T$, and the entries of the mass, damping, and stiffness matrices are given by

$$M_{11} = m_B z_B^2 + m_H z_H^2$$

$$M_{12} = -m_H u_H z_H$$

$$M_{21} = M_{12}$$

$$M_{22} = m_H u_H^2,$$

$$\begin{aligned}
C_{11} &= 0 \\
C_{12} &= -(m_B x_B z_B + m_H x_H z_H) \cos \lambda / w \\
C_{21} &= 0 \\
C_{22} &= (m_H u_H x_H) \cos \lambda / w,
\end{aligned}$$

$$\begin{aligned}
K_{011} &= m_B z_B + m_H z_H \\
K_{012} &= -m_H u_H \\
K_{021} &= K_{012} \\
K_{022} &= -m_H u_H \sin \lambda
\end{aligned}$$

and

$$\begin{aligned}
K_{211} &= 0 \\
K_{212} &= -(m_B z_B + m_H z_H) \cos \lambda / w \\
K_{221} &= 0 \\
K_{222} &= m_H u_H \cos \lambda / w
\end{aligned}$$

respectively.

The cyclic coordinates, which determine the bicycle's (rear contact point) position and orientation, can be recovered a posteriori by integrating the nonholonomic constraint (4.93). The machine position can then be tracked by integrating

$$\dot{x}_P = u \cos \psi \quad \dot{y}_P = u \sin \psi; \quad (4.94)$$

small angles are not assumed.

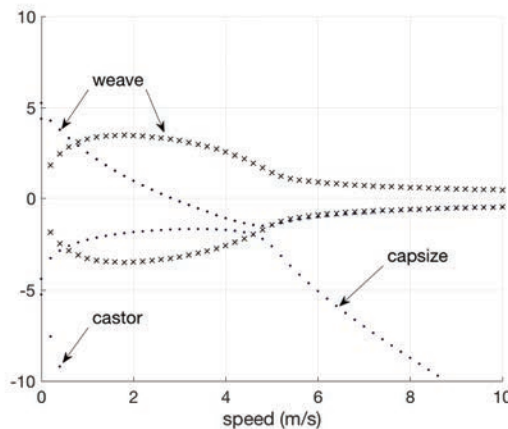


Figure 4.13: Stability properties of the primitive lumped-mass bicycle. The speed is varied from 0 to 10 m/s. The real parts of the eigenvalues are shown as dots, while the imaginary parts are shown as crosses.

Figure 4.13 shows the speed-dependent eigenvalues of the primitive bicycle that are computed using the characteristic equation associated with (4.93). The four zero-speed eigenvalues are located at ± 5.2484 and ± 4.3834 corresponding to inverted-pendulum-type capsize modes involving the whole machine and the steering assembly. The two unstable zero-speed modes immediately coalesce to form the so-called *weave mode*, which appears as a mixed roll-steer (fishtailing) oscillation. The two stable modes become the stable dynamic capsize mode and a (stable) castor mode. As the plot shows, this machine is stable for speeds above 2.8 m/s.

4.5 Wheel shimmy

Wheel shimmy can occur in everyday equipment such as shopping trolleys, wheeled stretchers, and wheelchairs. More important from our point of view is the occurrence of shimmy-related phenomena in road vehicles. The wheel shimmy modes in aircraft landing gear, automotive steering systems, and single-track vehicles can be violent and may lead to equipment damage and/or accidents. In March 1989 the left-hand main landing gear of a Fokker 100 aircraft failed in the landing at Geneva airport. From theoretical and experimental considerations it was concluded that any two-wheeled ‘F.28-like’ landing gear is essentially unstable [170]. Another comprehensive study of landing gear shimmy can be found in [87]. Original records of accelerations in high-speed hands-on bicycle shimmy are given in [86], which highlight how bicycle wobble (or shimmy) can be a frightening and dangerous phenomenon. The results show that shimmy is not attributable solely to the bicycle, but depends also on the rider. Another study of bicycle shimmy with experiments is given in [85]. The effect of frame compliance and rider mobility on scooter stability is investigated in [84]. In this work particular attention is paid to the wobble mode, because it may become unstable within the vehicle speed range. This article includes a summary of previous work and discusses the results of both numerical and experimental analyses. In practical situations these phenomena are complex and demand an analysis based on automated multibody modelling tools.

Castor systems comprise a spinning wheel, a kingpin bearing, and enough mechanical trail to provide a self-centring steering action. Our purpose here is to demonstrate that oscillatory instabilities can occur in relatively simple castor systems.

4.5.1 Simple case

A simple castor system commonly employed to demonstrate wheel shimmy, both experimentally and theoretically [8, 171], is shown in Figure 4.14. The wheel is axisymmetric and free to spin relative to its support forks; the wheel is deemed to have no spin inertia. The vertical moment of inertia of the wheel, fork, and kingpin assembly about its mass centre is J_z . The castor assembly is free to rotate around the kingpin through angle δ . The wheel has mechanical trail e and mass centre offset f with respect to the vertical kingpin bearing. The kingpin is free to translate laterally with displacement y from static equilibrium, while the whole assembly moves forward with constant speed v . The kingpin mounting has stiffness k , while the moving assembly has mass m .

Significant from the point of view of single-track vehicles, and aircraft nose-wheels, is the lateral compliance at the kingpin. If this compliance allows the assembly to rotate

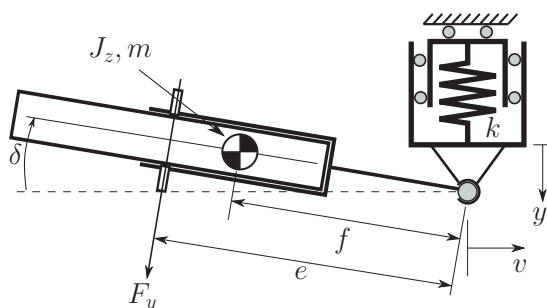


Figure 4.14: Plan view of a simple system capable of shimmy behaviours.

in roll about an axis well above the ground, as with a typical bicycle or motorcycle frame or aircraft fuselage, lateral motions of the wheel assembly are accompanied by camber changes. If, in addition, the wheel has spin inertia, gyroscopic effects come into play and may have an important influence on the shimmy behaviour. These effects are shown in [8] to create a second area of instability in the (v, e) space at higher speeds; v is the speed and e the mechanical trail. This phenomenon is known as ‘gyroscopic shimmy’; gyroscopic shimmy has also been described as a by-product of wheel hop in rigid-axle road cars [172]. In a rigid-axle car, a steer angle velocity combines with the wheel angular momentum to produce a gyroscopic moment in the roll axis direction that couples the steer velocity with wheel hop: ‘In this (shimmy) cycle, the tyre always meets the ground toed inwards, is swerved outward vigorously by the aligning torque, and is thrown into the air again toed out ready for the cycle to be repeated by the other wheel of the pair.’ Olley [172] further asserts that the prevention of shimmy is a strong motivator for the introduction of independent front suspensions: ‘Independent suspension simply inserts the entire sprung mass of the vehicle as a barrier between the two front wheels, so that the gyroscopic torque set up by the forced precession of one front wheel cannot be communicated to the other except through this mass.’

We will begin our study of shimmy with a system in which gyroscopic influences are absent. For small values of y and δ the equations of motion for the system in Figure 4.14 are found easily using Newton–Euler vector mechanics methods. To begin, we balance forces in the y -direction to obtain

$$m(\ddot{y} - f\ddot{\delta}) + ky - F_y = 0, \quad (4.95)$$

in which F_y represents the lateral tyre force. The tyre’s (aligning) moment M_z has been neglected for simplicity. Next, we use a moment balance around the castor assembly mass centre to obtain

$$J_z\ddot{\delta} + (e - f)F_y + kyf = 0. \quad (4.96)$$

In order to model the tyre force we will use a simple slip-based model; see Chapter 3. The castor ground contact point velocity component orthogonal to the wheel plane is

$$V_{Sy} = \dot{y} - v\delta - e\dot{\delta}.$$

Table 4.3 Parameter values (in SI units) for the simple castor system illustrated in Figure 4.14.

J_z	m	e	f	k	σ	C_α
1.0	30.0	0.12	0.08	45,000	0.1	4,500

The lateral tyre slip angle is defined as

$$\alpha = -\frac{V_{Sy}}{v} = \delta + \frac{e\dot{\delta} - \dot{y}}{v}, \quad (4.97)$$

with the corresponding lateral tyre force given by the differential equation

$$\frac{\sigma}{v}\dot{F}_y + F_y = C_\alpha\alpha, \quad (4.98)$$

in which C_α is the tyre's cornering stiffness and σ its relaxation length (a space constant related to the delay in the force-generation mechanism); for present purposes C_α and σ can be treated as fixed tyre-related parameters. If we take Laplace transform of (4.95), (4.96), and (4.98) and assemble them into a single matrix equation, one obtains

$$\begin{bmatrix} ms^2 + k & -fms^2 & -1 \\ kf & s^2J_z & e - f \\ C_\alpha s/v & -C_\alpha(1 + es/v) & 1 + \sigma s/v \end{bmatrix} \begin{bmatrix} y(s) \\ \delta(s) \\ F_y(s) \end{bmatrix} = 0, \quad (4.99)$$

with the system's characteristic equation given by the quintic polynomial

$$P(s) = \det \left(\begin{bmatrix} ms^2 + k & -fms^2 & -1 \\ kf & s^2J_z & e - f \\ C_\alpha s/v & -C_\alpha(1 + es/v) & 1 + \sigma s/v \end{bmatrix} \right). \quad (4.100)$$

Suppose the parameters for the simple castor system are those given in Table 4.3. Since the characteristic polynomial (4.100) is quintic, one expects five speed-dependent root loci. This is indeed the case as is shown in Figure 4.15 (a)—the plot is symmetric with respect to the horizontal axis. There is one stable real locus, a high-frequency locus with a resonant frequency in the range 5.97–8.75 Hz, and an unstable low-frequency mode with resonant frequency in the range 2.86–3.85 Hz. This unstable low-frequency mode is the castor shimmy mode.

To better understand these modes we will now consider three special cases. In the first we consider the limit

$$\begin{aligned} \lim_{C_\alpha \rightarrow \infty} \frac{P(s)}{Ck} &= a_3s^3 + a_2s^2 + a_2s^2 + a_1s + a_0 \\ &= \frac{(m(e-f)^2 + J_z)s^3}{kv} + \frac{m(e-f)s^2}{k} + \frac{e^2s}{v} + e, \end{aligned} \quad (4.101)$$

which corresponds to the case when the tyre's cornering stiffness goes to infinity thereby enforcing nonholonomic rolling. Assuming positive values for all the parameters and the speed, it follows from the Routh–Hurwitz criterion that the system will be stable provided $a_i > 0$ and

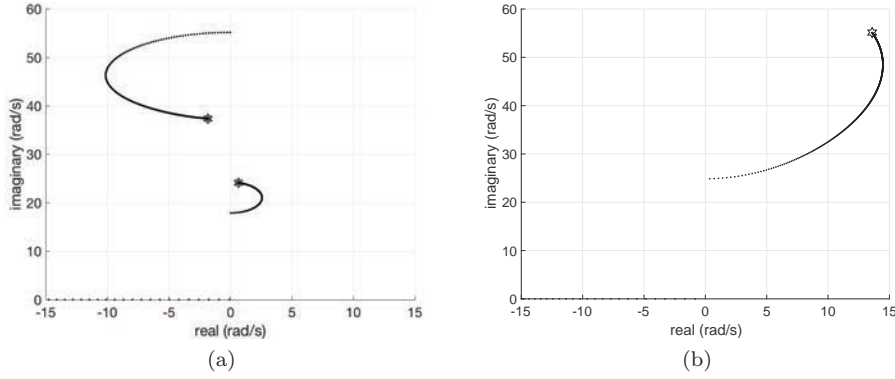


Figure 4.15: Speed-dependent root loci of the simple castor system shown in Figure 4.14. The speed is swept from 0 to 60 m/s; the hexagons corresponds to the high-speed end of the locus. The (a) figure represents the baseline configuration, while (b) represents the case with infinite cornering stiffness C_α .

$$\det \left(\begin{bmatrix} a_1 & a_0 \\ a_3 & a_2 \end{bmatrix} \right) = \frac{e}{vk} (mf(e-f) - J_z) > 0. \quad (4.102)$$

If condition (4.102) is satisfied, then $a_2 > 0$ is automatically satisfied. This illustrates the role played by the steering system geometry, and the mass and inertia properties of the moving assembly, in determining the stability, or otherwise, of the system. A root-locus plot for the infinite tyre cornering stiffness case with the parameter values given in Table 4.3 is shown in Figure 4.15 (b). Since condition (4.102) is not satisfied, an unstable system is predicted. The low-speed resonant frequency of the oscillatory mode in this system is of the order $25 \text{ rad/s} \approx 4.0 \text{ Hz}$, which matches that of the low-frequency mode in Figure 4.15 (a). The limit case in which $mf(e-f) = J_z$ is interesting. Using the fact that in this limit case the characteristic polynomial (4.101) must be of the form

$$\begin{aligned} a_3 s^3 + a_2 s^2 + a_2 s^2 + a_1 s + a_0 &= a_3 (s+p)(s^2 + \omega^2) \\ &= a_3 s^3 + a_3 p s^2 + a_3 \omega^2 s + a_3 p \omega^2, \end{aligned}$$

where p is an unknown real root and ω an unknown resonant frequency. By equating coefficients in like powers of s , one can deduce that

$$\omega = \sqrt{ke / (m(e-f))}. \quad (4.103)$$

As expected, the kingpin stiffness, the mass of the castor assembly, and the castor geometry all influence the frequency of oscillation. The mass distribution $mf(e-f) = J_z$ ensures that the kingpin is at the centre of percussion for the tyre force,⁹ and thus

⁹ This can be verified by solving (4.95) and (4.96) for δ and J_z in the case that $y = \ddot{y} = 0$.

the rolling constraint produces no force of reaction at the kingpin. Direct calculation using (4.95), (4.96), and $mf(e - f) = J_z$ gives

$$m\ddot{y} + \frac{key}{e - f} = 0, \quad (4.104)$$

reinforcing the fact that $\omega = \sqrt{ke/(m(e - f))}$.

In the second special case we consider

$$\begin{aligned} \lim_{k \rightarrow \infty} \frac{P(s)}{Ck} &= b_3 s^3 + b_2 s^2 + b_1 s + b_0 \\ &= \frac{\sigma(f^2 m + J_z)s^3}{Cv} + \frac{(f^2 m + J_z)s^2}{C} + \frac{e^2 s}{v} + e, \end{aligned} \quad (4.105)$$

which corresponds to a stiff castor assembly. Assuming positive values for the speed and parameters, it follows from the Routh–Hurwitz criterion that the system will be stable provided $b_i > 0$ and

$$\det \left(\begin{bmatrix} b_1 & b_0 \\ b_3 & b_2 \end{bmatrix} \right) = e(e - \sigma) \frac{f^2 m + J_z}{C_\alpha v} > 0, \quad (4.106)$$

or that $e > \sigma$. In other words, shimmy cannot occur when the trail e is greater than the relaxation length σ . For smaller (and still positive) trail the system is oscillatory unstable (shimmy), while for negative trail the system is divergent unstable.¹⁰ A root-locus plot for the stiff structure case with the parameter values given in Table 4.3 is shown in Figure 4.16 (a). Since condition (4.106) is satisfied, a stable system is predicted. After conversion to the Laplace transform domain, (4.97) and (4.98) give

$$F_y(s) = C_\alpha \left(\frac{v + se}{v + s\sigma} \right) \delta(s) \quad (4.107)$$

since $y(s) = 0$, which shows that stability in this case requires phase lead between $\delta(s)$ and the tyre force $F_y(s)$. In the limiting case that $e = \sigma$, $F_y = C_\alpha \delta$, which can be substituted into (4.95) and (4.96) to obtain

$$(J_z + mf^2)\ddot{\delta} + eC_\alpha \delta = 0. \quad (4.108)$$

This shows that the resonant frequency is given by

$$\omega = \sqrt{eC_\alpha/(J_z + mf^2)}. \quad (4.109)$$

In this case the tyre properties dictate both the conditions under which shimmy occurs and its frequency. The tyre relaxation length determines the onset, or otherwise, of shimmy, while the frequency of oscillation is dictated by the tyre's cornering stiffness.

¹⁰ In the case the tyre aligning moment $M'_z = -tF_y$ is included, where t is the pneumatic trail, the divergent instability appears for negative trail lower than $-t$.

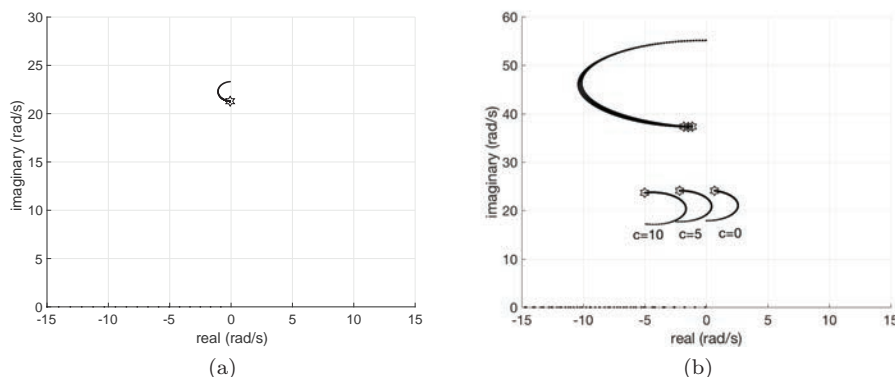


Figure 4.16: Root loci of the castor system shown in Figure 4.14 when (a) the castor has an infinite stiffness k , and (b) when a steer damper with different damping coefficients c is introduced. The speed is swept from 0 to 60 m/s with the hexagon at the high-speed end of the locus.

The Pirelli company reports on a tyre tester that relies on this result [173]. The test tyre is mounted in a fork trailing a rigidly mounted kingpin bearing and runs against a spinning drum to represent movement along a road. Following an initial steer displacement of the wheel assembly, the exponentially decaying steering vibrations are recorded, and the decrement yields the tyre relaxation length, while the frequency yields the cornering stiffness. Unlike other situations, the shimmy frequency is independent of speed.

In a third case, we consider a stiff castor assembly operating in concert with a stiff tyre. In the limit that both C_α and k go to infinity, both (4.101) and (4.105) give

$$P(s) = ekC_\alpha \left(\frac{es}{v} + 1 \right). \quad (4.110)$$

Importantly, shimmy cannot occur in this case when $e > 0$, since $P(s)$ has no right-half-plane roots. Under nonholonomic rolling conditions, following Laplace transformation, (4.97) gives

$$0 = \left(\frac{e}{v}s + 1 \right) \delta(s), \quad (4.111)$$

since the slip is zero.

As will soon be expanded on, a standard preventive measure for shimmy is the introduction of a castor assembly damper. This introduces a $c\dot{\delta}$ term in (4.96), where c is the castor damping coefficient. The stabilizing influence of this damper can be seen in Figure 4.16 (b). It is clear from this figure that the castor assembly with no damper has an unstable shimmy mode for all speeds. In the case that $c = 5 \text{ Nm s/rad}$, the castor assembly is stable at low and high speeds, while becoming unstable at intermediate speeds. When $c = 10 \text{ Nm s/rad}$, the shimmy mode is stable over the entire examined speed range. When damping is not included, the stability of the simple model is speed independent.

4.5.2 A more realistic setup

In this section we consider a steering system that resembles the front end of a bicycle, or motorcycle with a flexible frame. This system represents a self-centring castor assembly that is capable of shimmy—in this case gyroscopic influences will be present. The castor system in Figure 4.17 includes a twist axis SO with an associated twist angle ϕ ; the twist axis is inclined at angle ϵ to the horizontal. The wheel assembly is free to rotate around a steering axis through angle δ . To make the modelling conceptually easier, we will assume the axis system $Oxyz$ is inertial with its origin located at O , which is at the junction of the twist and steer axes. The castor assembly is stationary with no translational freedoms, and the road moves backwards at speed v . The x -axis of $Oxyz$ is aligned with the twist axis, its y -axis points out of the page, and its z -axis is specified by $\mathbf{z} = \mathbf{x} \times \mathbf{y}$, which is aligned with the steer axis. The unit vectors \mathbf{x} and \mathbf{y} are aligned with the x - and y -axes respectively (in $Oxyz$). The castor-fixed axis system $Ox'y'z'$ rotates through ϕ around the twist axis, and through angle δ around the steering axis. The wheel and wheel mount assembly has mass m_f , with its mass centre located at G , which has coordinates $(x_f, 0, z_f)$ in $Ox'y'z'$. The steer moment of inertia of the wheel frame assembly is I_{fz} (around G). The wheel has its centre at C , radius r_w , and spin inertia I_w . The wheel contacts the ground at P and the tyre is assumed to have no longitudinal slip and so $\dot{\xi} = -v/r_w$, where ξ is the castor spin angle.

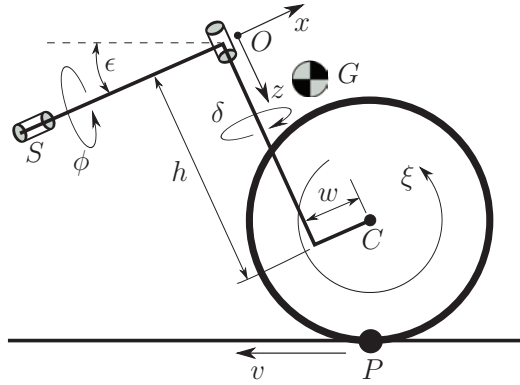


Figure 4.17: Castor with an inclined flexible mounting.

The equations of motion can be obtained using momentum-balancing arguments. Balancing the angular momentum around the twist axis (for small steer and twist angles) gives:

$$\begin{aligned} (I_{fx} + m_f z_f^2) \ddot{\phi} &= m_f z_f x_f \ddot{\delta} + g m_f c_\epsilon (x_f \delta - z_f \phi) - (h + r_w c_\epsilon) F_y \\ &\quad - k_p \phi - \frac{v I_w \dot{\delta}}{r_w}. \end{aligned} \quad (4.112)$$

The term on the left of (4.112) represents the moment due to the moment of inertia of

the wheel mount assembly around the twist axis. The first term on the right-hand side of (4.112) is a product-of-inertia term. The second term on the right is a gravitational moment term. The third term is the moment produced by the tyre side force F_y . The fourth term is the twist-axis restoring moment, while the fifth and final term is a gyroscopic moment.

Balancing the angular momentum, for small steer and twist angles, around the steer axis gives

$$(I_{fz} + x_f^2 m_f) \ddot{\delta} = m_f x_f z_f \ddot{\phi} + g m_f s_\epsilon (x_f \delta - z_f \phi) + (w - r_w s_\epsilon) F_y + \frac{v I_w \dot{\phi}}{r_w}. \quad (4.113)$$

The term on the left of (4.113) represents the moment of inertia of the wheel mount assembly around the twist axis (note the use of the parallel axis theorem), while the first term on the right-hand side of (4.113) is a product-of-inertia term. The second term on the right is a gravitational moment term. The third term is the moment produced by the tyre side force F_y , while the final term is a gyroscopic moment.

The tyre side force is generated from the side-slip and camber angles as follows,

$$F_y + \frac{\sigma}{v} \dot{F}_y = C_\alpha \left(\frac{\dot{\phi}}{v} (h + r_w c_\epsilon) + \frac{\dot{\delta}}{v} (r_w s_\epsilon - w) + c_\epsilon \delta - s_\epsilon \phi \right) + C_\gamma (c_\epsilon \phi + s_\epsilon \delta). \quad (4.114)$$

The coefficient of the cornering stiffness C_α is the side-slip, while the coefficient of tyre's camber stiffness C_γ is the tyre's camber angle.

After taking Laplace transforms, equations (4.112), (4.113), and (4.114) can be combined to gives the characteristic matrix

$$H(s) = \begin{bmatrix} s^2(I_{fx} + m_f z_f^2) + g m_f z_f c_\epsilon + k_p & \frac{sv I_w}{r_w} - s^2 m_f x_f z_f - g m_f x_f c_\epsilon & h + r_w c_\epsilon \\ \frac{sv I_w}{r_w} - g m_f z_f s_\epsilon + s^2 m_f x_f z_f & -s^2(I_{fz} + x_f^2 m_f) + g m_f x_f s_\epsilon & w - r_w s_\epsilon \\ C_\alpha \left(s_\epsilon - \frac{s(h + r_w c_\epsilon)}{v} \right) - C_\gamma c_\epsilon & C_\alpha \left(-c_\epsilon + \frac{s(w - r_w s_\epsilon)}{v} \right) - C_\gamma s_\epsilon & \frac{s\sigma}{v} + 1 \end{bmatrix} \quad (4.115)$$

in which s is the Laplace transform variable. The determinant of $H(s)$ is a quintic (in the Laplace variable s) with speed-dependent coefficients. A steering damper can be introduced by including a $-c_s \dot{\delta}$ term on the right-hand side of (4.113), and a corresponding $-s c_s$ term to the (2,2) entry of (4.115), in which c_s is the steering damping coefficient. The five roots of $\det H(s)$ determine the system's stability. The parameters for the castor system considered here are given in Table 4.4.

Figure 4.18 shows the locus of the speed-dependent roots of $\det H(s)$ as a function of speed. In common with Figure 4.15, this figure has a single stable real root and

Table 4.4 Parameter set for the included castor.

$C_\alpha = 1500 \text{ N/rad}$	$C_\gamma = 150 \text{ N/rad}$	$h = 0.6 \text{ m}$	$I_w = 0.25 \text{ kgm}^2$
$I_{fz} = 0.1 \text{ kgm}^2$	$k_p = 1.0 \times 10^4 \text{ Nm/rad}$	$m_f = 15.0 \text{ kg}$	$r_w = 0.3 \text{ m}$
$\sigma = 0.1 \text{ m}$	$w = 0.1 \text{ m}$	$\epsilon = 0.45 \text{ rad}$	$x_f = 0.1 \text{ m}$
$z_f = 0.3 \text{ m}$	$g = 9.806 \text{ m}^2$	$I_{fx} = 1.0 \text{ kgm}^2$	

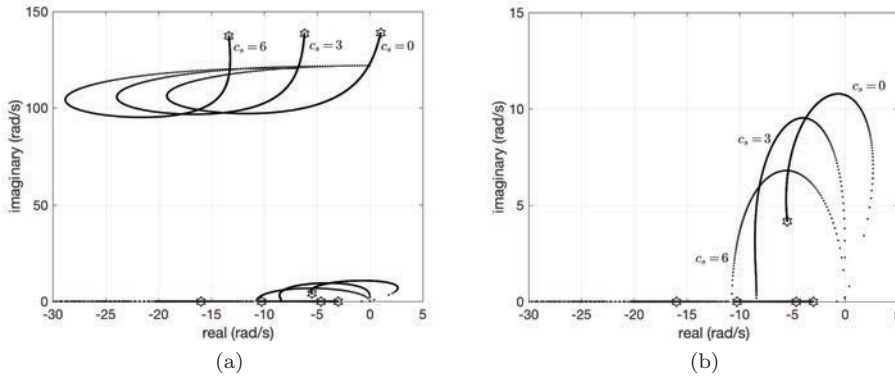


Figure 4.18: (a) Root loci for the inclined castor system derived from (4.115); only the roots with nonnegative imaginary part are shown. The speed is swept from 0 to 80 m/s, with a hexagon marking the high-speed end of the complex loci. Steering damper values of $c_s = 0$ Nm/s, $c_s = 3$ Nm/s and $c_s = 6$ Nm/s are shown. (b) is a zoom view of the low-frequency shimmy mode.

two pairs of complex conjugate loci. The high-frequency locus, which begins on the imaginary axis at 122 rad/s (19.4 Hz), moves into the left-half plane as the wheel's angular velocity increases, and then becomes unstable at high speed with a frequency of 137 rad/s (21.8 Hz). The real locus also moves into the left-half plane as the speed increases. The low-frequency shimmy locus is more interesting from an engineering perspective and potentially more troublesome, because it is unstable over a large range of speeds. Figure 4.19 (b) is an expanded view of the shimmy loci in Figure 4.19 (a) for three different steering damper values. The (a) locus is the zero steering damper case, which is unstable for speeds between 0.1 m/s and 8.05 m/s. A damper of 3 Nm/s is introduced in the (b) locus with the system marginally stable at low speed. Finally, in the (c) locus a damper of 6 Nm/s is introduced, which stabilizes the shimmy mode over the entire speed range.

The angular displacement components (ϕ and δ) of the three modes are shown in Figure 4.19, which have been scaled so that the steer component δ is unity. In the case of the shimmy mode (a) the frame and steer perturbations are almost in phase with the magnitude of the frame twist angle roughly half that of the steer angle. In the case of the stable real mode (b) the frame and steer are in phase with the frame twist angle magnitude approximately 25 % of the steer angle magnitude. In the case of the high-frequency mode (c) the frame and steer perturbations are almost in anti-phase with the magnitude of the frame twist angle and roughly 15 % of the steer angle. The system stability is now speed dependent, whereas with the simple model it was not.

Reconciliation with the simple case. We will now reconcile, briefly, some of the features of the castor system in Figure 4.14 with those in the more complex system in Figure 4.17. To do this we begin by setting $\epsilon = 0$ in (4.115) to obtain

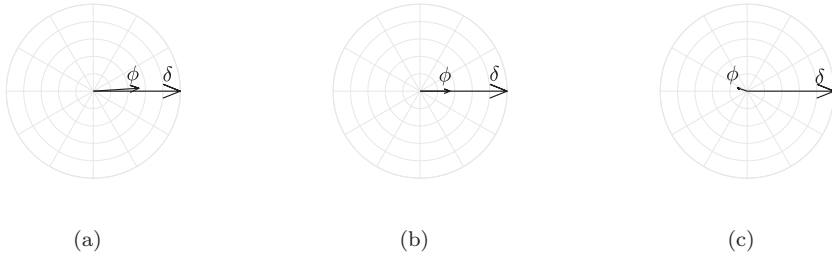


Figure 4.19: Mode shapes for the inclined castor system derived from (4.115) at 5 m/s and $c_s = 0$ Nm/s. The steering angle component (δ) of the mode shape is normalized to unity, with the castor assembly twist angle (ϕ) scaled the same way. Figure (a) is the unstable low-frequency shimmy mode in which δ and ϕ oscillate (almost) in phase at 1.64 Hz. Figure (b) is the stable real mode in which the twist angles δ and ϕ converge in phase. Figure (c) is the stable high-frequency shimmy mode in which δ and ϕ oscillate in approximate anti-phase at 18.9 Hz.

$$H(s) = \begin{bmatrix} s^2(I_{fx} + m_f z_f^2) + g m_f z_f + k_p & \frac{svI_w}{r_w} - s^2 m_f x_f z_f - g m_f x_f & h + r_w \\ \frac{svI_w}{r_w} + s^2 m_f x_f z_f & -s^2(I_{fz} + x_f^2 m_f) & w \\ -sC_\alpha \left(\frac{h+r_w}{v} \right) - C_\gamma & C_\alpha \left(\frac{sw}{v} - 1 \right) & \frac{s\sigma}{v} + 1 \end{bmatrix}. \quad (4.116)$$

In the case of ‘stiff’ mounting assemblies the difference between the translational structural freedom in Figure 4.14 and the rotational structural freedom in Figure 4.17 is immaterial. If the assembly in Figure 4.17 is deemed stiff, the system stability is determined by

$$\lim_{k_p \rightarrow \infty} \det(-H(s)/(k_p C_\alpha)) = \frac{\sigma(I_{fz} + m_f x_f^2)}{vC_\alpha} s^3 + \frac{I_{fz} + m_f x_f^2}{C_\alpha} s^2 + \frac{w^2}{v} s - w. \quad (4.117)$$

The first thing one observes is that w must be negative in order to achieve stable motion. This corresponds to the familiar ‘flip’ one observes when beginning to push a shopping trolley that has one of its castors pointing forwards. Once all the polynomial coefficients have the same sign, one requires

$$\det \left(\begin{bmatrix} a_1 & a_0 \\ a_3 & a_2 \end{bmatrix} \right) = \frac{w(I_{fz} + m_f x_f^2)}{vC_\alpha} (\sigma + w) > 0 \quad (4.118)$$

as a result of the Routh–Hurwitz criterion, which is the same as saying $-w > \sigma$, with $w < 0$. This condition matches exactly the stability criterion given in (4.106). In the limit case that $\sigma = -w$, the frequency of oscillation is

$$\omega = \sqrt{\frac{\sigma C_\alpha}{I_{fz} + m_f x_f^2}}, \quad (4.119)$$

which matches the expression given in (4.109). In the case where a ‘stiff’ castor assembly combines with a non-slipping tyre there obtains

$$\det(H(s)) = w\left(s\frac{w}{v} - 1\right), \quad (4.120)$$

which is stable for any $w < 0$. As with the simple configuration studied earlier, shimmy is not possible if the mount assembly is stiff and the tyre is non-slipping.

4.6 Unicycle

The unicycle is a human-powered, single-track, single-wheeled road vehicle that is more a plaything for the enthusiast than a practical means of transport. A number of wheel-based commuter devices have evolved from the rolling disc as it is described in Section 2.10. From a transport perspective the rolling disc's most direct descendant is the BC wheel, which is simply a wheel with pegs extending on either side of the wheel axle. In order to ride it you 'simply' balance on the pegs as the wheel is rolling. The name comes from the popular comic strip, *B.C.* by Johnny Hart, in which the characters commute by rolling on large stone wheels. The BC wheel is the most basic form of unicycle.

As was the case with the development of the bicycle, the next evolutionary step was the 'ultimate wheel', which includes pedals on either side of the wheel. This machine has no frame or seat but provides a means of introducing a propulsive moment. The vertical dynamics of this machine is obviously akin to the inverted pendulum with vertical stability control coming from the rider twisting and turning their body.

A conventional unicycle is illustrated in Figure 4.20. The machine has two components: a wheel and a rigid frame. The frame is free to yaw, roll, and pitch. Although the wheel shares common yaw and roll angles with the frame, it is free to spin relative to the frame. As is suggested by the sketch, the rider can be separated into a lower body that will be considered part of the frame and rigidly attached to it, while the rider's upper body that can 'swivel' relative to the lower body through additional yaw, roll, and pitch angular freedoms. This motion can be considered constrained by active control torques and passive structural spring-damper constraints. The road-wheel interaction can be modelled using a slipping tyre that generates longitudinal and lateral forces, and aligning and overturning moments. The road-wheel interaction can be modelled alternatively using nonholonomic constraints.



Figure 4.20: Unicycle and rider; picture taken from [174].

Scholarly articles on unicycle dynamics appear to be concentrated in the control systems literature. As a consequence of its inherent instability, the unicycle is considered a system worthy of study in a closed-loop control context [175–177]. The unicycle has been used as a case study in the development of autonomous robots, and in the emulation of human riding [174]. The unicycle has been used as an exemplar vehicle in tracking and motion-control studies [178], and in the study of the stabilization of non-holonomic systems [179]. Due to its presumed simplicity, the unicycle has been used in the study of nonlinear cyclic pursuit problems [180]. From a mechanics modelling perspective, this literature has a common shortcoming—the dynamic modelling of the vehicle is often simplistic.

A correct and interesting treatment of the unicycle can be found in [181]. Although the equations of motion were derived using multibody modelling software, they are not difficult to interpret in a classical Newton–Euler framework. Unlike any other treatment that the authors are aware of, realistic tyre forces and moments are given in the model presented. In the tyre description longitudinal-, lateral-, and turn-slips and, through them, shear forces and steering moment, and the rolling velocity are all included. The theory and results described provide a predictive capability for robotic unicycles, which can be used to guide the design of these machines.